Tribologically induced nanolaminate in a cold-sprayed WC-reinforced Cu matrix composite: a key to high wear resistance

Yinyin Zhang[1,2], Deep Choudhuri[3], Thomas W. Scharf[3], Sylvie Descartes[2*], Richard R. Chromik[1*]

[1]Department of Mining and Materials Engineering, McGill University, 3610 University Street, Montreal, QC, H3A 0C5, Canada

[2]Univ Lyon, INSA-Lyon, CNRS UMR5259, LaMCoS, F-69621, France

[3]Department of Materials Science and Engineering, University of North Texas, Denton, TX 76203-5310, USA

[*]Corresponding authors: richard.chromik@mcgill.ca (Richard R. Chromik)
sylvie.descartes@insa-lyon.fr (Sylvie Descartes)

Abstract

A self-organized 2D nanolaminate with an average lamella thickness of ~22 nm was formed in the subsurface of a cold-sprayed WC-reinforced metal matrix composite (MMC) Cu-MoS_2-WC during oscillatory sliding and it was responsible for the much more stable friction and improved wear resistance. Using high resolution transmission electron microscopy and nanoindentation, three important characteristics were observed in the nanolamellae that contributed to their great stability and high hardness. First, misorientation of the lamellar boundaries was low i.e. <3°. Second, stacking faults and twins were main substructures. Lastly, the recrystallization was controlled by grain boundary nucleation, that required much higher driving force than triple junction nucleation. Such nanolaminate eliminated massive detachment and permitted small detached particles that tended to be trapped in the contact and experienced rapid recrystallization. The equiaxed nanograins on the top surface accommodated shear force by grain boundary-mediated deformation mechanisms, which could potentially benefit tribological performance. Observations of the tribologically induced microstructural evolutions near the surface showed the formation of self-organized tribomaterial with high hardness and stability, which was aided by the presence of WC particles. Considering the effectiveness of these microstructures, future design of wear resistant alloys may consider engineering these microstructures in the as-prepared state.

Key words: oscillatory sliding wear, ceramic reinforced metal matrix composite, 2D nanolamellae, wear resistance

1 Introduction

Tribological loading of metallic materials leads to many surface and subsurface modifications to the microstructure and chemical composition, including but not limited to, microstructural refinement induced by severe plastic deformation, and phase transformation owing to interaction with the environment [1-5]. Such modifications contribute to the formation of a continuous or patchy layer, often called tribomaterial or tribologically transformed structure (TTS) in the literature, from which wear particles are produced to form third bodies [6, 7]. For example, Greiner et al. [8] carried out a mild reciprocating sliding test on a OFHC copper sliding against sapphire and found amorphous or nanocrystalline clusters comprising elevated oxygen content formed just below the worn surface after only 100 cycles. Sliding contacts on alloys showed formation of non-equilibrium solid solution due to interactions between the rubbing surfaces and the environment [9]. For spinodal hardened Cu-15 wt.% Ni- 8 wt.% Sn bronze sliding against stainless steel, the subsurface layer transformed to a composite of Cu-rich solid solution containing equiaxed grains with an average grain size of 6.7 nm and $(Fe, Cr)_2O_3$ dispersions, which resulted from bronze dealloying, oxidation, severe plastic deformation and turbulent mixing. Such self-organized nanocrystalline solid solution or nanocomposites (i.e. solid solution + oxide precipitates) presented high hardness, and often led to much improved wear resistance [2, 10]. Therefore, one factor determining wear resistance is the ability of the material to form a near-surface microstructure that is stable with good mechanical properties [2].

To obtain enhanced wear resistance for metals, one often turns to metal matrix composites (MMCs), where common theories show link of load-bearing capacity to wear resistance. However, recent studies of tribology of these materials have shown rapid formation of wear resistant tribomaterial near the worn surface and indicate MMCs may be a route for obtaining self-organized microstructures that are exceptionally wear resistant [5, 11-13]. For example, Shockley et al. [5] reported that during sliding of a cold-sprayed aluminum matrix composite (Al + 22wt% Al_2O_3) against sapphire, a layer with a thickness of 3-5 µm was formed onto the worn surface and it consisted of nanocrystalline grains of 5-20 nm that were embedded in an amorphous matrix. However, without reinforcing alumina, the subsurface layer was filled with grains as large as 750 nm. The former tribomaterial suppressed

significantly crack initiation and resulted in a continuous but slower material transfer at the contact compared to the latter case, where there was discontinuous detachment of large chunks of material. Consequently, that leads to much more stable friction and a wear rate that was around one order of magnitude lower than the unreinforced aluminum. Presence of ceramic particles produced high strain localization in the vicinity of hard particles at the near surface, and triggered extreme microstructure refinement in this layer. In the meantime, the homogeneous distribution of high oxygen in this layer suggested its incorporation into the aluminum crystal lattice, which was a possible formation of a non-equilibrium supersaturated solid solution [5]. As such, MMCs often presented significantly higher hardness of the subsurface layer and much better wear resistance.

Even though ceramic reinforced MMCs obtained the above advantages, which can be utilized to design wear resistant materials and make it possible to control wear under a wide range of running conditions such as contact pressure, sliding speed, running temperature, and humidity, some fundamental questions i.e. formation, deformation mechanisms and strengthening mechanisms of those tribomaterials under tribological loading have not been well understood so far. In the present work, the above research questions were studied by producing wear resistant tribomaterial at contacting surface of a cold-sprayed Cu matrix composite (i.e. Cu-MoS_2-WC) sliding against stainless steel (AISI 440C).

Cold spray was selected because it is a solid-state deposition process, where feedstock powders are accelerated to very high speeds in a range of 500-1200 m/s by a high pressure gas stream at a temperature that is often below the melting point of feedstock material, thus formation of coatings occurs mainly due to kinetic energy of the particles [14]. Because high temperature is not involved, some common problems encountered in thermal spray such as severe oxidation, decomposition, unwanted phase transformation, as well as thermal residual stress can be minimized or eliminated [14]. Therefore, it is ideal for spraying oxygen-sensitive materials like copper, aluminum, titanium, and phase-sensitive materials like carbides and solid lubricants [15]. Cu and bronze MMCs reinforced by ceramics and/or solid lubricants, that are widely used as bearing materials to achieve low friction, low wear and high corrosion resistance for automotive and aerospace applications, have been successfully fabricated by cold spray [16-18]. Incorporation of alumina to Cu and bronze effectively reduced wear rate during dry sliding wear tests [17, 18]. Bronze + 13% alumina produced by cold spray achieved even lower wear loss than bronze + 32% alumina fabricated by plasma spray [17].

Previous work by the authors [19] showed under a normal load of 150 N, the Cu-MoS_2-WC composite had more stable friction and much improved wear resistance compared to the unreinforced Cu-MoS_2 (i.e. ~80×10^{-6} mm^3/Nm vs. ~210×10^{-6} mm^3/Nm). The improved performance was due to the presence of 12% WC that facilitated formation of cohesive tribomaterial to prevent massive detachment. In this study, using high resolution transmission electron microscopy (HRTEM) and nanoindentation techniques, we studied the microstructure and mechanical properties of the wear-resistant tribomaterial, as well as its evolution to wear particles. Finally, the role of the microstructure and properties of the tribomaterial plays on the improved wear resistance of ceramic reinforced MMCs was discussed.

2 Materials and experimental

2.1 Cold spray deposition

The Cu-MoS_2-WC composite was fabricated using a commercial cold spray system (PCS800, Plasma Giken, Japan) with a mix of spherical Cu powder (Tekna Advanced Materials Inc., d_{50} = 26 µm) and 5 wt.% of flake-like MoS_2 powder (Climax, d_{50} = 30 µm), and 19 wt.% WC (Tekna Advanced Materials Inc., d_{50} = 30 µm). The feedstock was mechanically admixed for 1 h. Fractions of each component in the blend were chosen to gain an acceptable deposition efficiency based on empirical practice [19]. Chemical composition of Cu is shown in Table 1. The composite was deposited on an aluminum alloy (AA6061) substrate and it was ~3 mm thick after 3 passes. Nitrogen was used as carrying gas and the gas temperature and pressure were set at 800 °C and 5 MPa, respectively. More details on the cold spray process can be found in our previous work [19-21]. Recovery of MoS_2 and WC in the Cu-MoS_2-WC were ~2.2 wt.% and ~12 wt.%, respectively. Cross sectional micrographs of the composites are shown in Fig. 1A-B. The composites are dense (i.e. porosity ~0.2%), and MoS_2 was deposited along the Cu particles. Previous studies by the authors demonstrate no phase transformation or chemical change occurred during cold spray [21, 22]. Fig. 1C-D show detailed cold-sprayed Cu microstructure before being subjected to oscillatory sliding wear. The microstructural refinement from coarse grains (i.e. over 10 µm) in the feedstock powder to cold-sprayed coating was observed explicitly elsewhere [22]. Since the metallic particles are accelerated to ultra-sonic speed and then impact onto the substrate, the deformed Cu consists of relatively coarse structure that is originally located in the center of the particle, and

refined structure that is close to the particle edge where dynamic recrystallization was believed to take place [23]. Therefore, the cold-sprayed Cu comprises a wide range of grain sizes from ~10 µm to 100-200 nm [22].

Table 1 Chemical composition (wt.%) of Cu

Cu	Sn	Al	Ag	Ni	K	O
>99.6	0.32	<0.01	<0.01	<0.01	<0.01	0.067

2.2 Oscillatory sliding wear test

A custom-built ball-on-plate tribometer (Laboratoire de Mecanique des Contacts et des Structures at INSA de Lyon, France) was used to perform oscillatory wear tests. The upper counterface is stationary while the lower plate vibrates with a small amplitude of displacement. Stainless steel (AISI 440C) ball with a radius of 50 mm was used as the counterface. A normal load of 150 N was applied and the other parameters were designed to achieve gross slip contact condition. More details on contact condition identification can be found in [19, 24]. The imposed slip amplitude δ^* was ± 200 µm, the oscillating frequency was 5 Hz. The tests were performed in an ambient temperature of 20 - 25 °C and a relative humidity of 30-50%. Prior to sliding wear tests, the specimens were precisely machined to a dimension of 12 (length) × 8 (width) × 5.8 mm (height) using electrical discharge machining, and the thickness of the cold-sprayed composites was reduced to ~2 mm. They were then mechanically polished using water based 9- and 3-µm diamond suspensions, resulting in a surface roughness (Ra) of ~0.3 µm. To observe subsurface microstructure and third body at steady state, microstructure observations were performed on the specimens after 30,000-cycle sliding.

2.3 Microstructure characterization

Locations for microstructural observations were selected according to the sliding loops during test. A typical loop that plots tangential force (Q) versus sliding amplitude (δ), shown in Fig.2A, was quasi-rectangular, indicating gross slip condition [25, 26]. The actual sliding amplitude was around 125 µm. Coupled with Hertzian contact area (contact radius a_r = 400 µm), a theoretical contact was drawn in Fig. 2B and the total contact during sliding was roughly 1050 µm. Top view of the contact is schematically shown in Fig. 2C, at the center of which is an area that was always in

contact and thus had no or very limited direct exposure to air during the test. Three foils for transmission electron microscopy (TEM) were made from areas that are marked in Fig. 2B-C using small rectangles. Two of them (the black and white rectangles) were from center of the contact, the third (the red rectangle) was from the area that was more to the outside region of the contact where it was exposed to air. The locations are also shown from a cross sectional micrograph of the wear scar (Fig. 2D). Here the direction normal to the sliding plane is defined as ND, and those along and perpendicular to the sliding direction in the sliding plane are SD and TD, respectively. SD-ND cross sectional micrographs and energy dispersive X-ray spectroscopy (EDX) scans were acquired by a scanning electron microscope (SU-8230, Hitachi, Japan), while the TEM foils were made along TD-ND view of the wear track. Foil #1 was to examine microstructural characteristics of the wear-resistant subsurface microstructure, while foils #2 and #3 were for third body observations from the locations without and with air exposure, respectively. The TEM foils were prepared by a focused ion beam-scanning electron microscope (FIB-SEM, Helios NanolLab DualBeam, FEI, US) using the standard lift-out technique. A protective platinum stripe was deposited on the surface before FIB milling. Microstructures of the subsurface and third bodies were characterized by Tecnai G2-F20 TEM (FEI, US) at 200 kV.

Hardness and Young's modulus of the subsurface microstructure were studied by nanoindentation (Hysitron, Ubi3, USA) with a Berkovich diamond tip. Indentation tests were performed on mechanically polished cross-sections of the wear scars. The worn plate was firstly cut parallel to the sliding direction using a slow-speed diamond blade, then cold-mounted and mechanically ground and polished down to 0.05 µm by colloidal silica, and finally vibratory polished for 3 hours using colloidal silica to eliminate or minimize deformation induced by previous grinding and polishing. A load function of 5 s linear loading time to a peak load of 1 mN and 5 s linear unloading time was used for nanoindentation. Hardness values were calculated by Oliver and Pharr method [27] and the values reported in the present work were averages of 15 indents.

3 Results

Fig. 3A shows three distinct layers from cross section of the wear track, in which the WC particles have turned into small pieces and mixed thoroughly with the matrix material. From the top, there is a layer, ~3-8 µm thick, consisting of third body particles. Detailed microstructure of this layer

will be shown in Section 3.2. Below the third body layer is a 10 - 20 µm wear-resistant subsurface layer that has a laminated structure parallel to the sliding plane from both SD-ND and TD-ND cross sections (Fig. 3A&B). Therefore, the wear-resistant subsurface microstructure consists of two-dimensional lamellae. Underneath this layer is ultrafine Cu grains (UFG) with a sharp interface with them. In Fig. 3C, the UFGs are mostly equiaxed grains with an average size of ~ 400 nm and shear bands that are roughly parallel to the sliding surface. An EDX scan across the lamellae and UFGs (Fig. 3D) exhibits negligible oxygen content in both microstructures, indicating no detectable oxidation or oxygen-rich solid solution formed during sliding test.

3.1 Wear-resistant subsurface microstructure at the Cu-MoS_2-WC contact

A small area marked as a white rectangle in Fig. 3B was explicitly investigated because of the thinner foil on the left side that permitted high quality micrographs. From Fig. 4A-B, lamella boundaries are nearly, not exactly, parallel to the sliding surface, which is most likely due to the WC particle nearby that deviated material flow during plastic deformation. In Fig. 4C, the selected area electron diffraction pattern (SAED) demonstrates the 2D lamellae are Cu, suggesting no phase transformation occurred inside this layer. The elongated diffraction spots in the SAED indicate a strong crystallographic texture with the (111) planes aligned along the sliding surface, which is a typical texture component in FCC metals subjected to simple shear deformation [28]. The continuous rings from the SAED pattern reveal presence of randomly-orientated nanograins that suggests fragmentation or dynamic recrystallization took place. Thickness of the lamellae measured by linear intercept method ranges from 3 to 130 nm with an average value of ~22 nm, while the length of the lamellae extends over 10 µm (Fig. 3A-B), resulting in an aspect ratio >100. In fact, the lamellae from TD-ND view often exhibit more fragmentation than that from SD-ND cross section; for instance, the aspect ratio of a nanolamellar Ni produced by mechanical grinding was ~100 from SD-ND view yet only ~10 from the TD-ND cross section [29]. In Fig. 4E, the dark contrast in the lamella interior indicates presence of dislocations or subgrain boundaries. Note that twinning was not found at this magnification, implying twinning did not occur predominately at this length scale (i.e. a few tens of nanometers), even though it was one of the primary deformation mechanisms of Cu over some severe plastic deformations, in particular at cryogenic temperatures [30-32]. The rest of this Section is to observe more closely the deformed microstructures by HRTEM.

In Fig. 5, two typical lamellae are captured, labeled as I and II, and they are around 20 nm and 15 nm in thickness, respectively. The boundary (marked by white arrows) between adjacent lamellae was examined by HRTEM observations. From the inverse fast Fourier transformation (IFFT) of a portion of the boundary (Fig. 5B), a very small misorientation of around 2.2° exists between the planes in lamella I and II. Misorientation of the lamella boundaries between I and II are low and range from 0.8° to 2.6°. More lamellae were analyzed carefully, and the boundaries are less than 3° in misorientation between two adjacent lamellae. Two spots at the lamella interior of I and II are selected and their IFFT images (Fig. 5C-F) show a small misorientation ~2° between the planes in I, indicating misorientation gradient inside the lamella probably caused by geometrically necessary dislocations (i.e. the dark contrast in the lamella I), while 0° inclination in II. Note that no stacking faults or deformation twins were observed in those lamellae.

The second feature of the nanolamellar structure resides in the lamellae that exhibit a wavy grain boundary (Fig. 6A). Stacking faults and thin deformation twins are frequently observed in the lamella interior. Boundaries of those defects are often parallel to one another, as well as to the lamella boundary. The IFFT image of region B in Fig. 6A confirms the defect boundary is a stacking fault that passes only a few atom planes. The HRTEM image of region C shows formation of a thin twin with a thickness of ~1 nm.

As mentioned earlier, the laminated structure also contains randomly-orientated nanograins that are likely a result of dynamic recrystallization. As shown in Fig. 7A, the lamella is characterized by the presence of a bulge that has been subdivided from the parent lamella by stacking faults, which is confirmed by the FFT and IFFT of region C (Fig. 7C). A new nanograin (marked by red dash lines) that is roughly ellipsoid, ~5-10 nm, nucleates at the triple junction of the lamella boundary and the stacking faults. In Fig. 7B, a bulge along the lamella boundary is separated from the parent lamella by twinning whose boundary (white arrowed) is parallel to the long axis of the lamella. A new ellipsoid-shaped grain, ~5 nm in short axis and ~15 nm in long axis, is formed at the joint of the lamella boundary and twin boundary. Stacking faults are found aside the twin boundary and extending to bulge interior. Note that in this micrograph, only one side of the lamella boundary was identified; the other one is either far below or does not show due to image quality.

3.2 Mechanical property of the wear-resistant subsurface microstructure

Hardness of the lamellar structure determined by nanoindentation is as high as 3.83 ± 0.28 GPa, much higher than the most refined microstructure found in the Cu-MoS_2 subsurface (i.e. 3.0 ± 0.4 GPa [19]). The Young's modulus was measured as 128.8 ± 13.6 GPa, consistent with previous measurements on nanocrystalline Cu, which is in a range of 110 – 130 GPa [33]. It is worth to note that negligible pileups were formed beside the indents, and it is probably because the subsurface was plastically deformed microstructure. Morphology of the indents (Fig. 8A) were taken by SEM to help select data points that landed on Cu and were not affected by the embedded WC fragments.

In order to explore size-dependent strengthening mechanisms, it was necessary to conduct side experiments that led to different microstructural length scales than the nanolamellae. The same cold-sprayed specimens were subjected to sliding wear testing and post-annealing (see S1 for their microstructure), and their hardness values as a function of the inverse square root of the grain size are plotted in Fig. 8B; the hardness of the nanolamellar structure is included for comparison by considering the average lamellar thickness as equivalent grain size. The hardness data fits fairly well a conventional Hall-Petch relationship, and it shows the same slope as the Hall-Petch relationship for the nanograins of high purity Cu (Cu > 99.99%) manufactured via different techniques reported in the literature [33, 34] [35]. The higher intercept observed here for the H-P fit is most likely associated with the minor alloying elements in Cu (see Table 1).

Following the strategy used by Rupert et al. [36], the nanolaminated structure was also indented with a cube corner diamond indenter at a constant strain rate up to a peak load of 10 mN, which intentionally generated indents with pileup. In Fig. 8C, the morphology of a residual cube-corner indents is shown and several shear steps are observed that are roughly along the lamella boundary and stand out of the deformed surface. Also, the step thickness is comparable to the thickness of the lamellae. This indicates the lamellae probably shear apart from each other, giving rise to such incompatible deformation behavior.

3.3 Microstructure of detached particles at the center of the wear scar

As shown in Fig. 9A-B, at the wear track center where the area was not directly exposed to air throughout the test, there exists a third body layer, 5-7 μm thick, comprised of agglomerates that exhibit a high diversity on morphology and size (i.e. ~ 0.2 - 3 μm). Presence of agglomerates, the large ones in particular, implies strong adhesion between detached particles when they were not

exposed to air, as well as possible rolling movement during sliding, as stated in [37]. Formation of this layer is analyzed explicitly in Section 4.2, while here we focus on microstructure features of the agglomerates of detached particles.

Fig. 9C shows microstructures near a lamella boundary, a feature remained from the nanolamellae from which the particles were detached. The left-side lamella was divided into small blocks, and right-side lamella was even further refined into equiaxed grains (< 5 nm in size). The disparate grain refinement from lamella to lamella rendered local inhomogeneity of third body particles at this stage. The left-side lamella was then observed more closely as it most likely represents an early stage of microstructural evolution after detachment. The small blocks adjacent to the lamella boundary are elongated, around 15 nm in long axis, 5 nm in short axis. Inverse FFT images (Fig. 9D-E) of selected areas in an elongated block reveal a small orientation gradient of around 2° inside the grain, indicating a small lattice distortion inside the grains. Misorientation of the grain boundaries marked in Fig. 9C are all high angle grain boundaries (~30°-60°). Although there are probably some low angle grain boundaries available that we did not capture by quite a few HRTEM images, their population ought to be low. Triple junctions were found to be preferential nucleation sites, as shown in Fig. 9F, where a dislocation-free grain, 5-10 nm in size, was formed and surrounded by high angle grain boundaries.

In the lamella interior, the grain refinement proceeded continuously across the entire lamella. In Fig. 10A, a lamella of ~25 nm thick, even though the boundaries are still visible, is filled with 2-3 layers of refined grains, whose boundaries are highlighted in Fig. 10B. Those grains are varying in morphology and size; some of them are equiaxed while the others are slightly elongated, with a size range of 5 - 15 nm. Given that the grain boundaries newly formed inside the lamella are mostly above 15°, as noted in Fig. 10B, the grains are randomly orientated; combining the fact that no stacking faults and twins were detected, the texture and substructures that were observed previously in the subsurface were erased once the material was detached and became third bodies.

Another characteristic microstructure in the third body particles was found at the edge of the agglomerates that was adjacent to pores, where air could be trapped during the test. In Fig. 10C, a thin layer of around 20 nm thick contains nanograins, mostly less than 5 nm in size, that are well spheroidized and distributed in an amorphous matrix. Note that few relatively large elongated

grains that are 5-15 nm are also found inside this layer. Even though no higher oxygen content was detected using EDS equipped inside the TEM, the distinct feature next to a pore reveals that oxygen could accelerate microstructural refinement and amorphization, as is demonstrated in Section 3.4.

3.4 Microstructure of third bodies exposed to air

Around 100 µm away from the contact center, another TEM foil (foil #3 in Fig. 2D) was made by FIB along TD-ND cross section to examine microstructural evolution of the third body when it was exposed to air directly during sliding tests. As shown in Fig. 11A, a continuous and compact third body layer, around 280 nm thick, formed on the topmost of the worn surface. Although it appears as a weak lamellar structure, in particular at the bottom of the layer, the SAED pattern demonstrates randomly orientated nanograins with no sign of preferred orientation; a bright field TEM image (Fig. 11B) confirms this layer consists of equiaxed nanograins with homogenously distributed grain sizes, showing a sharp yet cohesive interface with the underneath microstructure, where the grains are mostly equiaxed and a few hundred nanometers in size. Note that the SAED pattern (inset of Fig. 11B) taken from the third body layer indicates it is a mix of nanocrystalline Cu (not indexed) and a small amount of Cu_2O (indexed). Thirty-five measurements on grain sizes from HRTEM micrographs demonstrate the nanocrystalline grains are in a range of 2.5 - 8 nm with an average diameter of 5.5 nm.

Deformation mechanisms and interaction of those nanocrystalline grains were observed using HRTEM images. In Fig. 11C, the FFT of grains I and II, ~3-5 nm in size, illustrates the plane distance is around 0.25 nm, corresponding to (111) lattice of Cu. Using FFT (inset of Fig. 11C) and inversed FFT image of the grains (Fig. 11D), the misorientation between grains I and II was approximately 20°. A perfect dislocation (marked by "T") and an array of partial dislocations (noted by an arrow behind the "T") were formed at the grain boundary to accommodate deformation. This could be a result of grain boundary rotation by dislocation climbing at grain boundary [38].

Inside other nanograins (~6 - 8 nm), as illustrated in Fig. 11E, stacking faults (indicated by the white polylines) were generated to accommodate deformation induced by the sliding motion. Inside the grain III, there is a high number of stacking faults that do not cross the entire grain but stop in the grain interior, leaving partial dislocations at the front of them, noted as an arrow. It is

evident that those stacking faults nucleated at the grain boundary and then grew into grain interior by partial dislocation emission.

Remarkably, neighbouring grains of IV and V align along the dashed arrow (Fig. 11F), a sign of formation of shear bands. This implies grain boundary sliding could take place in the later stage by sliding over the coplanar arrays of grain boundaries [39]. In addition, Moiré patterns are observed among the nanograins (see Fig. 11F) and their directions are rather random, which suggest the material was under stress [40-42]. Worth to point out that Moiré patterns are often viewed when two closely spaced arrays of lines differ in either spacing or orientation, and therefore they are used to describe strain and stress fields of a specimen under pressure [42].

4 Discussion

4.1 The nanolamellar Cu at Cu-MoS_2-WC contact and comparisons to conventional severe plastic deformations

In the present study, a nanolaminated Cu with an average lamella thickness of ~22 nm and low grain boundary misorientation (<3°) was produced in the subsurface of an oscillatory sliding contact, where large plastic strain and high strain gradient were developed [43, 44]. Therefore, the subsurface microstructure evolution can be reasonably considered as one type of severe plastic deformation. Even so, the nanolamellae here are different from layered structures obtained from conventional severe plastic deformations (SPDs) that often produce submicrometer-sized elongated grains with mostly high angle grain boundaries [45]. For instance, equal-channel angular pressing (ECAP) processed Cu gave elongated grains with a thickness of around 200 nm after one pass and it remained constant with more passes up to 12, yet the fraction of high angle grain boundaries increased up to 50% [46]. Since SPD performed at low temperatures hinders or inhibits dislocation annihilation and thus further reduces grain sizes to some extent, a surface severe plastic deformation applied on copper in liquid nitrogen rendered nanolaminated grains only inside well-developed shear bands and those nanolamellae had a mean transverse boundary spacing of ~46 nm and low angle grain boundaries of ~7.4° [30], a slightly larger scale compared to the microstructures in the present study. In addition, it is interesting to note that even though similar 2D lamellae were produced successfully by means of a surface mechanical grinding treatment

(SMGT) in Ni and a body-centred cubic (bcc) interstitial-free steel [29, 47], no such large volume of nanolaminated structure was formed in Cu when it was subjected to SMGT [48], nor other surface treatments such as surface mechanical attrition [49], high pressure scratch [50], and shot peening [51]. Therefore, one important novel result of the present work is the formation and stabilization of the 2D nanolaminated Cu by oscillatory sliding wear of the cold-sprayed WC-reinforced composite against AISI 440C.

According to literature, high strain gradient generated at the sample surface by plastic deformation is a crucial factor to produce nanolaminated metals, because high strain gradient requires accumulation and storage of geometrically necessary dislocations (GNDs) [29, 47]. For the present oscillatory sliding contact, the accumulation of subsurface plastic strain (δ) can be determined by microstructural change, specifically grain boundary deflection and grain size refinement by a ratio: $\delta = \frac{D}{(\sqrt{3})c}$, where D is initial grain size before sliding wear test, c is refined grain size in the subsurface of the wear track [52]. The mean grain size in the unworn cold-sprayed Cu-WC-MoS_2 composite was measured as ~2 µm (Fig. 1D-E) and the average lamella boundary spacing in the subsurface layer was ~22 nm; a shear strain of ~60 was achieved inside this layer. Given that it is 10-20 µm thick, the strain gradient is therefore estimated as 3-6 μm^{-1}, at least one order of magnitude higher than it occurs in high pressure torsion (HPT) processing of Cu under a typical condition: a disk with a radius of 5 mm, initial thickness 1 mm, and final thickness of 0.13 mm after 5 turns, yields a strain gradient of ~0.2 μm^{-1} at the radius of 3 mm [53]. Since GND density (ρ_{GND}) is proportional to the strain gradient (x), i.e. $\rho_{GND} = \frac{4x}{(\sqrt{3})b}$, where b is the Burgers vector (b ≈ 0.256 nm for Cu), the GND density in the nanolaminated structure is then approximately 2.5-5×10^{16} m^{-2}, that is significantly higher than that processed by ECAP (i.e. on the order of 10^{15} m^{-2} the maximum) [54], and slightly higher than Cu treated by dynamic plastic deformation (DPD) (i.e. 1.8-3.6 × 10^{16} m^{-2}) [30]. Consequently, a high strain gradient generated underneath the oscillatory sliding contact facilitated rapid formation and accumulation of GNDs to form the dramatically refined nanolamellae.

An important difference between the Cu-MoS_2-WC in the present study and materials reviewed above from conventional SPD processes is that the WC particles were involved during deformation. Hard second-phase particles effectively raise strain gradient around them to maintain

deformation compatibility, leading to a high density of geometrically necessary dislocations (GNDs) that readily form grain boundaries [55, 56]. Thus, they are a key factor to produce such high strain gradient in the subsurface layer. Moreover, the second-phase particles may block grain boundary migration that help to overcome grain size saturation and stabilize the grain boundaries. Saturation of grain refinement by SPDs was predominantly a result of grain boundary migration and dislocation annihilation when metals deformed to large strains [45]. This was commonly found in single-phase metallic materials; for instance, after 12 passes of pure copper processed by ECAP, the cell size kept constant at 150 - 200 nm and was no longer further refined [54]. Addition of second-phase particles can effectively stabilize grain boundary and thus further refine microstructure. A copper matrix nanocomposite Cu+0.5wt.%Al_2O_3 processed by HPT yielded nanograins ~80 nm, much finer than that of HPT pure Cu whose grain size often saturated at submicrometers [57]. Therefore, for Cu-MoS_2-WC contact, the WC fragments distributed inside the subsurface layer enabled to accumulate dislocations, build up high strain gradient around them, and stabilize grain boundary, and hence transform the UFG Cu to nanometer size ~22 nm. Apparently, the above process was governed by dislocation slip rather than deformation twinning, which agrees well with the nanolaminated copper found inside the shear bands processed by the dynamic plastic deformation conducted in liquid nitrogen [30].

Three microstructural characteristics are believed to be responsible for the high stability of the present nanolaminated Cu. First, the low misorientation of the lamella boundaries (Fig. 5) is more stable than high angle grain boundaries against recovery and recrystallization. It has been shown that nanolaminated Ni with low-angle grain boundaries had a higher onset temperature of coarsening (~506°C) than that of nanograined nickel with mostly high angle grain boundaries (~443°C) [58]. Moreover, the low misorientation indicates the lamella boundaries have low energy, and it is probably because they have been exposed to sliding-induced heating for a long time (~1.5 h). This low temperature process is called grain boundary relaxation and the thermal annealing annihilated excess dislocations inside grain boundaries, that were often observed in nanograined microstructures, without measurable change in grain size or texture, resulting in more equilibrium and stable grain boundaries with regularly spaced dislocations [36, 59].

Second, stacking faults and twins found inside some of the lamellae are low-energy boundaries comparing to high angle grain boundaries, and thus have high thermal stability [60]. The third

mechanism to stabilize the nanolamellae in the subsurface layer is the unique nucleation mode of recrystallization. Even though low misorientation and low energy of the lamella boundary promoted high thermal stability, some boundaries were rough and developed into serrations that stacking faults or twin boundary could pass, forming a triple junction where a new grain could be nucleated. Therefore, the recrystallization inside lamellar structure contained two nucleation mechanisms that took place in a specific sequence: first, nucleation via grain boundary bulging, then new grains nucleated at the newly-formed triple junctions. As summarized in [61], nucleation taking place along the grain boundaries required a much higher driving force than that occurring at triple junctions. For polycrystalline copper, nucleation at a triple junction commenced at a strain of ~0.01, only $\frac{1}{20}$ to $\frac{1}{10}$ of the peak strain; while the critical strain for nucleation along grain boundary was $\frac{1}{4}$ to $\frac{1}{2}$ of the peak strain [62, 63]. And the grain boundary nucleation also depended on grain boundary character and grain boundary mobility [62]. In the present study, since the grain boundary nucleation was required to form a triple junction, the overall recrystallization rate was controlled by the grain boundary nucleation. Therefore, recrystallization was effectively supressed, the lamellar structure was stabilized.

In addition, it is worth to note that no shear bands were found inside the nanolamellae, suggesting homogenous deformation in the subsurface layer, which is distinct from the unstable nanolaminate Cu obtained by ECAP + cold rolling in liquid nitrogen. A high population of shear bands were formed inside the lamellate and yielded a heterogeneous structure due to highly localized deformation. As a result, those shear bands triggered abnormal grain growth under low temperature annealing, displaying a poor stability [64].

Another characteristic of the nanolamellae is its high hardness that gave rise to the improved wear resistance. Because the hardness follows a H-P relationship (Fig. 8), the lamella boundary is as effective as high angle grain boundary in blocking dislocations, which is owing to the high stability of the lamella boundaries and strain hardening from the substructures (i.e. twins and stacking faults). The same result was obtained for nanolaminate Ni produced by surface mechanical grinding treatment (SMGT); the Vickers hardness of the ~20-nm lamellae in Ni was about 6.4 GPa that matched well the H-P relation [58].

4.2 Third bodies in the contact

As the precursor of third body, the subsurface material controlled the microstructure and morphology of third body particles that then determined third body rheology and third body flows at the sliding contact. Our previous work has showed such wear-resistant tribomaterial, i.e. nanolamellae, favoured stable and small volume of third body flows, i.e. material transfer and ejection, leading to improved wear resistance compared to its unreinforced counterparts [19]. Therefore, it is interesting to explore microstructure transformation from the nanolamellae to nanocrystals that were observed in the third bodies. In this section, two questions will be answered that are associated with third-body microstructure. First, how do the nanolamellae transform to equiaxed nanocrystalline grains? Second, what are deformation mechanisms of the nanocomposites under sliding?

4.2.1 Detached particles at the center of the contact

After the nanolaminate Cu detached and became a third body particle trapped in the contact, further refinement took place by continuous dynamic recrystallization (cDRX), which was distinct from the discontinuous dynamic recrystallization (dDRX) occurred in the subsurface layer. The third body microstructure is characterized by the local heterogeneity at a length scale of one-lamella-thickness (~22 nm), suggesting large local diversity of stress and/or strain distribution inside even one particle. Hence the microstructure evolution is likely driven by large shear strain and great strain gradient that are localized. In literature, three possible mechanisms for nanoscale refinement of copper originated from laminate structure have been documented based on experimental observations: fragmentation of lamellae by forming high angle grain boundaries gradually, generation of secondary twins and shear banding [65]. According to Fig. 9-10, in which no twins or shear bands were detected, the latter two deformation modes can be easily ruled out. Given that almost all grain boundaries in the third body particle are high angle grain boundaries, without any strong sign of transition from low to high misorientation, we could probably exclude the first fragmentation mechanism as well. The main reason the above three deformation mechanisms are not perfectly suitable for the present case may reside in the difference in lamella boundaries: twin-matrix lamellae produced by SPDs in the literature while dislocation-based low misorientation lamella boundaries yielded in the present work.

As pointed out by Rigney et al. [66], microstructural evolution of the third body in the contact share strong similarities with that of metallic powders subjected to mechanical milling, because in both cases the metallic particles experience deformation, fracture, intimately mixing in the contact by repeated compression and shear. Early work of ball milling Cu observed formation of nanometer grains (i.e. 10-100 nm) and the nucleation started both at the shear bands, twin boundaries and grain boundaries [32]. Such refinement mechanism seemed to match better the present observations where all defects including stacking faults, twins seen in the subsurface layer were replaced by newly formed grains. In addition, alloying by surface contamination and oxygen was acknowledged to play an important role for the grain refinement [49]. That was most likely the reason why further refined grains were observed in third body particles that were adjacent to pores (Fig. 10C).

4.2.2 Third bodies exposed to air

Formation of nanograins less than 10 nm in size in the third body layer that was directly exposed to air during sliding is not surprising. However, the deformation mechanisms of those nanograins have not been clear thus far. Our detailed characterization revealed grain boundary mediated deformation mechanisms, which is consistent with observations of deformation mechanisms of grains at the same length-scale during other deformation modes such as tension [38]. Those deformation mechanisms include firstly, grain boundary rotation via dislocation climbing at the grain boundaries, the same as an in-situ TEM observation of a nanocrystalline platinum during tensile testing and such phenomenon was detected only when the grains were smaller than 6 nm [38]. Secondly, partial dislocation emission from grain boundaries, leaving behind stacking faults. In this case the grain boundaries act as dislocation source because grain interior is dislocation-free. This is often the first step to nucleate deformation twins, which was also observed in nanocrystalline Cu deformed at room temperature and a low strain rate [67]. Finally, it is interesting to see a preview of grain boundary sliding inside the nanocrystalline grains, as grain boundary sliding at elevated temperature produces superplasticity that could benefit tribological performance [68, 69]. Argibay et al. [69] documented that a low friction regime of metal-metal contacts was due to formation of a nanocrystalline surface film (~10 nm) that accommodated shear by grain boundary sliding.

A question remaining is interaction between the nanocrystalline grains and the amorphous matrix. One of the experimental difficulties could reside in a high-quality characterization of the interface of those two phases, as well as a lack of control on the size of nanograins and chemical composition of the amorphous matrix in a tribological condition. Deformation behaviour of crystalline-amorphous nanolaminates was explored through molecular dynamics simulations and the crystalline-amorphous interface was crucial to transfer dislocation plasticity initiated in crystals to the amorphous phase while avoiding microcracking, resulting in enhanced toughness of the composite [70]. However, their response to tribological loading is still an open question.

4.3 Improved wear resistance of ceramic reinforced MMCs

During steady state, WC reinforced composite exhibits more stable friction and much improved wear resistance comparing to unreinforced Cu-MoS_2 under a normal load of 150N [19], which was driven by the nanolamellar subsurface layer that exhibits high stability and high hardness. Despite nanograins are often formed at sliding contact, most, if not all, of them are refined and stabilized by oxidation and/or surface contamination, unlike the nanolamellar Cu in the present work [50, 71]. Apparently, WC fragments that distributed in the subsurface helped to overcome grain size saturation that was encountered commonly during conventional SPD techniques (e.g. HPT [45]), and further refined this layer down to ~22 nm by generating high strain and high strain gradient around themselves, as discussed in Section 4.1. Therefore, plastic strain and strain gradient achieved in the subsurface layer play an important role in resulted microstructure, and breakdown of the saturated grain size is crucial to gain high wear resistance at high contact pressure.

The second feature that the Cu-MoS_2-WC subsurface microstructure brought to potentially improve wear resistance is its heterogeneity. From Fig. 4, this layer contains a small amount of submicrometer lamellae, newly formed nanograins and defects such as stacking faults and twins, which could enhance ductility of the material. This phenomenon has been studied for a few decades on hetero-structured materials containing nano- and a larger-length scale structure that show a good combination of strength and ductility which cannot be obtained by homogeneous materials [68]. The better ductility supressed cracking and avoided detachment of a large volume of subsurface microstructure and therefore resulted in improved wear resistance.

The third contribution of the nanolaminate structure to the better wear resistance is that lamellar structure probably tended to have lower shear strength than equiaxed grains, such that plastic deformation concentrated in a shallow layer at the top surface, protecting the underneath material. Formation of shear steps on the pile-ups (see Fig. 8C) serves as indirect evidence that shear may occur preferentially along lamellar interface that is parallel to the sliding surface. What's more, the typical shearing texture with the (111) plane parallel to the sliding surface may produce lower shear strength comparing to other possible texture components. A similar sliding-induced texture of an alternating Cu and Ag nanolaminates was believed to hold a lower shear strength, in particular comparing to the Cu-Ag solid solution, and thus ended up with much improved wear resistance [72]. Both molecular dynamic (MD) simulation and experimental results of nanolaminated Cu//Nb indicated that Cu (111)//Nb (110) interface showed much lower shear strength than Cu (112)//Nb (112) [73, 74]. Although multiple-phase nanolamellar structures are not our focus of the present work, they provide a general idea on shear strength with different crystal orientations.

5 Conclusions

In summary, under a tribological loading of a cold-sprayed WC-reinforced Cu-MoS_2-WC sliding against AISI440C counterface at a normal force of 150N, a wear resistant subsurface layer formed and it consists of 2D nanolamellae with high hardness and great stability. Formation of such nanolaminate was mainly due to presence of WC particles that gave rise to steep strain gradients around them to accumulate and store dislocations during shearing. This facilitated microstructural refinement from UFG to the nanolaminate; in other words, WC helped to overcome structural saturation that was commonly observed in traditional SPDs. The high stability of the nanolaminate structure was originated from the low misorientation boundaries, relaxed and organized grain boundaries, as well as the unique recrystallization mode. The recrystallization was effectively supressed by grain boundary nucleation because it required much higher driving force than that nucleation at triple junctions. Such hard and stable subsurface microstructure was believed to be the key to the improved wear resistance. Therefore, formation of nanolamellae at the near surface of the contact provided a novel strategy for the design of wear resistant materials particularly applied at high normal pressure.

The nanolaminate effectively eliminated massive detachment and produced small particles that were trapped in the contact and underwent transformation from nanolamellae to equiaxed nanocrystalline grains. Grain refinement was proceeded rapidly by continuous dynamic recrystallization (cDRX). Local disparity of microstructure in the third body particle indicated the transformation was driven by highly local shear strain and participation of oxygen could accelerate grain refinement. A compact third body layer consisting of nanograins and amorphous was formed on the top surface. Deformation mechanisms of this layer were identified as grain boundary-mediated mechanisms including grain boundary rotation via dislocation climbing at grain boundaries, emission of partial dislocations from grain boundaries, as well as possible grain boundary-sliding. Those deformation mechanisms could potentially enhance tribological performance.

Acknowledgements

The authors gratefully acknowledge the financial support from Natural Sciences and Engineering Research Council (NSERC) of Canada and ANR INSA de Lyon. They gratefully acknowledge Dr. Xuedong Liu (McGill University), Victor Ageh (University of North Texas), and Lionel Lafarge (INSA Lyon) for technical assistance on TEM, FIB cut, and tribometer respectively, David Chern for assistance on nanoindentation, and Tekna Plasma Systems Inc. and Climax Molybdenum for donation of the powders.

References

1. Xin, L., Z. Wang, J. Li, Y. Lu, and T. Shoji, *Microstructural characterization of subsurface caused by fretting wear of Inconel 690TT alloy.* Materials Characterization, 2016. **115**(Supplement C): p. 32-38.
2. Singh, J.B., J.G. Wen, and P. Bellon, *Nanoscale characterization of the transfer layer formed during dry sliding of Cu–15wt.% Ni–8wt.% Sn bronze alloy.* Acta Materialia, 2008. **56**(13): p. 3053-3064.
3. Espallargas, N., A. Fischer, A. Igual Muñoz, S. Mischler, and M.A. Wimmer, *In-situ generated tribomaterial in metal/metal contacts: Current understanding and future implications for implants.* Biotribology, 2017. **10**: p. 42-50.
4. Shakhvorostov, D., B. Gleising, R. Büscher, W. Dudzinski, A. Fischer, and M. Scherge, *Microstructure of tribologically induced nanolayers produced at ultra-low wear rates.* Wear, 2007. **263**(7-12 SPEC. ISS.): p. 1259-1265.
5. Shockley, J.M., E.F. Rauch, R.R. Chromik, and S. Descartes, *TEM microanalysis of interfacial structures after dry sliding of cold sprayed Al-Al2O3.* Wear, 2017. **376-377**: p. 1411-1417.

6. Rigney, D.A. and S. Karthikeyan, *The Evolution of Tribomaterial During Sliding: A Brief Introduction.* Tribology Letters, 2010. **39**(1): p. 3-7.
7. Zhou, Z., E. Sauger, J. Liu, and L. Vincent, *Nucleation and early growth of tribologically transformed structure (TTS) induced by fretting.* Wear, 1997. **212**(1): p. 50-58.
8. Greiner, C., Z. Liu, L. Strassberger, and P. Gumbsch, *Sequence of Stages in the Microstructure Evolution in Copper under Mild Reciprocating Tribological Loading.* ACS Applied Materials & Interfaces, 2016. **8**(24): p. 15809-15819.
9. Singh, J., J.-G. Wen, and P. Bellon, *Nanoscale characterization of the transfer layer formed during dry sliding of Cu–15 wt.% Ni–8 wt.% Sn bronze alloy.* Acta Materialia, 2008. **56**(13): p. 3053-3064.
10. Cai, W. and P. Bellon, *Subsurface microstructure evolution and deformation mechanism of Ag–Cu eutectic alloy after dry sliding wear.* Wear, 2013. **303**(1): p. 602-610.
11. A. Alidokht, S., S. Yue, and R.R. Chromik, *Effect of WC morphology on dry sliding wear behavior of cold-sprayed Ni-WC composite coatings.* Surface and Coatings Technology, 2019. **357**: p. 849-863.
12. Alidokht, S.A., P. Manimunda, P. Vo, S. Yue, and R.R. Chromik, *Cold spray deposition of a Ni-WC composite coating and its dry sliding wear behavior.* Surface and Coatings Technology, 2016. **308**(Supplement C): p. 424-434.
13. Shockley, J.M., S. Descartes, P. Vo, E. Irissou, and R.R. Chromik, *The influence of Al2O3 particle morphology on the coating formation and dry sliding wear behavior of cold sprayed Al–Al2O3 composites.* Surface and Coatings Technology, 2015. **270**(Supplement C): p. 324-333.
14. Papyrin, A., V. Kosarev, S. Klinkov, A. Alkhimov, and V.M. Fomin, *Cold spray technology*. 2006: Elsevier.
15. Champagne, V.K., *The cold spray materials deposition process*. 2007: Elsevier.
16. Chen, W., Y. Yu, J. Cheng, S. Wang, S. Zhu, W. Liu, and J. Yang, *Microstructure, Mechanical Properties and Dry Sliding Wear Behavior of Cu-Al2O3-Graphite Solid-Lubricating Coatings Deposited by Low-Pressure Cold Spraying.* Journal of Thermal Spray Technology, 2018. **27**(8): p. 1652-1663.
17. Miguel, J.M., J.M. Guilemany, and S. Dosta, *Effect of the spraying process on the microstructure and tribological properties of bronze–alumina composite coatings.* Surface and Coatings Technology, 2010. **205**(7): p. 2184-2190.
18. Triantou, K.I., D.I. Pantelis, V. Guipont, and M. Jeandin, *Microstructure and tribological behavior of copper and composite copper+alumina cold sprayed coatings for various alumina contents.* Wear, 2015. **336-337**: p. 96-107.
19. Zhang, Y., S. Descartes, and R.R. Chromik, *Influence of WC on third body behaviour during fretting of cold-sprayed CuMoS2WC composites.* Tribology International, 2019. **134**: p. 15-25.
20. Zhang, Y., S. Descartes, P. Vo, and R.R. Chromik, *Cold-Sprayed Cu-MoS2 and Its Fretting Wear Behavior.* Journal of Thermal Spray Technology, 2015. **25**(3): p. 1-10.
21. Zhang, Y., J.M. Shockley, P. Vo, and R.R. Chromik, *Tribological Behavior of a Cold-Sprayed Cu–MoS2 Composite Coating During Dry Sliding Wear.* Tribology Letters, 2016. **62**(1): p. 1-12.
22. Zhang, Y., N. Brodusch, S. Descartes, R.R. Chromik, and R. Gauvin, *Microstructure refinement of cold-sprayed copper investigated by electron channeling contrast imaging.* Microscopy and Microanalysis, 2014. **20**(05): p. 1499-1506.

23. Zou, Y., W. Qin, E. Irissou, J.-G. Legoux, S. Yue, and J.A. Szpunar, *Dynamic recrystallization in the particle/particle interfacial region of cold-sprayed nickel coating: Electron backscatter diffraction characterization.* Scripta Materialia, 2009. **61**(9): p. 899-902.
24. Zhang, Y., S. Descartes, P. Vo, and R.R. Chromik, *Cold-Sprayed Cu-MoS2 and Its Fretting Wear Behavior.* Journal of Thermal Spray Technology, 2016. **25**(3): p. 473-482.
25. Vingsbo, O. and S. Söderberg, *On fretting maps.* Wear, 1988. **126**(2): p. 131-147.
26. Fouvry, S., P. Kapsa, and L. Vincent, *Analysis of sliding behaviour for fretting loadings: determination of transition criteria.* Wear, 1995. **185**(1-2): p. 35-46.
27. Oliver, W.C. and G.M. Pharr, *An improved technique for determining hardness and elastic modulus using load and displacement sensing indentation experiments.* Journal of materials research, 1992. **7**(06): p. 1564-1583.
28. Kocks, U.F., C.N. Tomé, H.-R. Wenk, and A.J. Beaudoin, *Texture and anisotropy: preferred orientations in polycrystals and their effect on materials properties*. 2000: Cambridge university press.
29. Liu, X.C., H.W. Zhang, and K. Lu, *Formation of nano-laminated structure in nickel by means of surface mechanical grinding treatment.* Acta Materialia, 2015. **96**: p. 24-36.
30. Yan, F., H. Zhang, N. Tao, and K. Lu, *Quantifying the microstructures of pure Cu subjected to dynamic plastic deformation at cryogenic temperature.* Journal of Materials Science & Technology, 2011. **27**(8): p. 673-679.
31. Li, Y.S., N.R. Tao, and K. Lu, *Microstructural evolution and nanostructure formation in copper during dynamic plastic deformation at cryogenic temperatures.* Acta Materialia, 2008. **56**(2): p. 230-241.
32. Huang, J., Y. Wu, and H. Ye, *Deformation structures in ball milled copper.* Acta materialia, 1996. **44**(3): p. 1211-1221.
33. Sanders, P.G., J.A. Eastman, and J.R. Weertman, *Elastic and tensile behavior of nanocrystalline copper and palladium.* Acta Materialia, 1997. **45**(10): p. 4019-4025.
34. Chen, J., L. Lu, and K. Lu, *Hardness and strain rate sensitivity of nanocrystalline Cu.* Scripta Materialia, 2006. **54**(11): p. 1913-1918.
35. Suryanarayanan, I.R., C.A. Frey, S.M.L. Sastry, B.E. Waller, and W.E. Buhro, Materials Science and Engineering: A, 1999. **264**.
36. Rupert, T.J., J.R. Trelewicz, and C.A. Schuh, *Grain boundary relaxation strengthening of nanocrystalline Ni–W alloys.* Journal of Materials Research, 2012. **27**(9): p. 1285-1294.
37. Berthier, Y., L. Vincent, and M. Godet, *Velocity accommodation in fretting.* Wear, 1988. **125**(1): p. 25-38.
38. Wang, L., J. Teng, P. Liu, A. Hirata, E. Ma, Z. Zhang, M. Chen, and X. Han, *Grain rotation mediated by grain boundary dislocations in nanocrystalline platinum.* Nature Communications, 2014. **5**: p. 4402.
39. Markmann, J., P. Bunzel, H. Rösner, K.W. Liu, K.A. Padmanabhan, R. Birringer, H. Gleiter, and J. Weissmüller, *Microstructure evolution during rolling of inert-gas condensed palladium.* Scripta Materialia, 2003. **49**(7): p. 637-644.
40. Qiao, J.W., Y. Zhang, P.K. Liaw, and G.L. Chen, *Micromechanisms of plastic deformation of a dendrite/Zr-based bulk-metallic-glass composite.* Scripta Materialia, 2009. **61**(11): p. 1087-1090.
41. Sciammarella, C.A., *The moiré method—a review.* Experimental Mechanics, 1982. **22**(11): p. 418-433.

42. Pipes, R.B., *Moire analysis of the interlaminar shear edge effect in laminated composites.* Journal of Composite Materials, 1971. **5**(2): p. 255-259.
43. Rigney, D.A., X.Y. Fu, J.E. Hammerberg, B.L. Holian, and M.L. Falk, *Examples of structural evolution during sliding and shear of ductile materials.* Scripta Materialia, 2003. **49**(10): p. 977-983.
44. Rigney, D., *Comments on the sliding wear of metals.* Tribology international, 1997. **30**(5): p. 361-367.
45. Pippan, R., S. Scheriau, A. Taylor, M. Hafok, A. Hohenwarter, and A. Bachmaier, *Saturation of Fragmentation During Severe Plastic Deformation.* Annual Review of Materials Research, 2010. **40**(1): p. 319-343.
46. Molodova, X., G. Gottstein, M. Winning, and R.J. Hellmig, *Thermal stability of ECAP processed pure copper.* Materials Science and Engineering: A, 2007. **460-461**: p. 204-213.
47. Liu, X.C., H.W. Zhang, and K. Lu, *Formation of nanolaminated structure in an interstitial-free steel.* Scripta Materialia, 2015. **95**: p. 54-57.
48. Li, W.L., N.R. Tao, and K. Lu, *Fabrication of a gradient nano-micro-structured surface layer on bulk copper by means of a surface mechanical grinding treatment.* Scripta Materialia, 2008. **59**(5): p. 546-549.
49. Wang, K., N. Tao, G. Liu, J. Lu, and K. Lu, *Plastic strain-induced grain refinement at the nanometer scale in copper.* Acta Materialia, 2006. **54**(19): p. 5281-5291.
50. Hughes, D.A. and N. Hansen, *Exploring the Limit of Dislocation Based Plasticity in Nanostructured Metals.* Physical Review Letters, 2014. **112**(13): p. 135504.
51. Wang, X., Y.S. Li, Q. Zhang, Y.H. Zhao, and Y.T. Zhu, *Gradient Structured Copper by Rotationally Accelerated Shot Peening.* Journal of Materials Science & Technology, 2017. **33**(7): p. 758-761.
52. Dautzenberg, J.H. and J.H. Zaat, *Quantitative determination of deformation by sliding wear.* Wear, 1973. **23**(1): p. 9-19.
53. Jiang, H., Y.T. Zhu, D.P. Butt, I.V. Alexandrov, and T.C. Lowe, *Microstructural evolution, microhardness and thermal stability of HPT-processed Cu.* Materials Science and Engineering: A, 2000. **290**(1-2): p. 128-138.
54. Dalla Torre, F., R. Lapovok, J. Sandlin, P.F. Thomson, C.H.J. Davies, and E.V. Pereloma, *Microstructures and properties of copper processed by equal channel angular extrusion for 1–16 passes.* Acta Materialia, 2004. **52**(16): p. 4819-4832.
55. Zhang, Y., N. Brodusch, S. Descartes, J.M. Shockley, R. Gauvin, and R.R. Chromik, *The effect of submicron second-phase particles on the rate of grain refinement in a copper-oxygen alloy during cold spray.* Journal of Thermal Spray Technology, 2017. **26**(7): p. 1509-1516.
56. Apps, P.J., J.R. Bowen, and P.B. Prangnell, *The effect of coarse second-phase particles on the rate of grain refinement during severe deformation processing.* Acta Materialia, 2003. **51**(10): p. 2811-2822.
57. Islamgaliev, R.K., W. Buchgraber, Y.R. Kolobov, N.M. Amirkhanov, A.V. Sergueeva, K.V. Ivanov, and G.P. Grabovetskaya, *Deformation behavior of Cu-based nanocomposite processed by severe plastic deformation.* Materials Science and Engineering: A, 2001. **319-321**: p. 872-876.
58. Liu, X.C., H.W. Zhang, and K. Lu, *Strain-Induced Ultrahard and Ultrastable Nanolaminated Structure in Nickel.* Science, 2013. **342**(6156): p. 337-340.

59. Jang, D. and M. Atzmon, *Grain-boundary relaxation and its effect on plasticity in nanocrystalline Fe.* Journal of Applied Physics, 2006. **99**(8): p. 083504.
60. Lu, K., *Stabilizing nanostructures in metals using grain and twin boundary architectures.* Nature Reviews Materials, 2016. **1**: p. 16019.
61. Sakai, T., A. Belyakov, R. Kaibyshev, H. Miura, and J.J. Jonas, *Dynamic and post-dynamic recrystallization under hot, cold and severe plastic deformation conditions.* Progress in Materials Science, 2014. **60**: p. 130-207.
62. Miura, H., T. Sakai, R. Mogawa, and J.J. Jonas, *Nucleation of dynamic recrystallization and variant selection in copper bicrystals.* Philosophical Magazine, 2007. **87**(27): p. 4197-4209.
63. Miura, H., T. Sakai, S. Andiarwanto, and J.J. Jonas, *Nucleation of dynamic recrystallization at triple junctions in polycrystalline copper.* Philosophical Magazine, 2005. **85**(23): p. 2653-2669.
64. Jiang, Y., R.C. Gu, Y. Zhang, and J.T. Wang, *Heterogeneous structure controlled by shear bands in partially recrystallized nano-laminated copper.* Materials Science and Engineering: A, 2018. **721**: p. 226-233.
65. Tao, N.R. and K. Lu, *Nanoscale structural refinement via deformation twinning in face-centered cubic metals.* Scripta Materialia, 2009. **60**(12): p. 1039-1043.
66. Rigney, D.A., L.H. Chen, M.G.S. Naylor, and A.R. Rosenfield, *Wear processes in sliding systems.* Wear, 1984. **100**(1): p. 195-219.
67. Liao, X.Z., Y.H. Zhao, S.G. Srinivasan, Y.T. Zhu, R.Z. Valiev, and D.V. Gunderov, *Deformation twinning in nanocrystalline copper at room temperature and low strain rate.* Applied Physics Letters, 2004. **84**(4): p. 592-594.
68. Ovid'ko, I.A., R.Z. Valiev, and Y.T. Zhu, *Review on superior strength and enhanced ductility of metallic nanomaterials.* Progress in Materials Science, 2018. **94**: p. 462-540.
69. Argibay, N., M. Chandross, S. Cheng, and J.R. Michael, *Linking microstructural evolution and macro-scale friction behavior in metals.* Journal of Materials Science, 2017. **52**(5): p. 2780-2799.
70. Cheng, B. and J.R. Trelewicz, *Mechanistic coupling of dislocation and shear transformation zone plasticity in crystalline-amorphous nanolaminates.* Acta Materialia, 2016. **117**: p. 293-305.
71. Xin, L., B.B. Yang, Z.H. Wang, J. Li, Y.H. Lu, and T. Shoji, *Microstructural evolution of subsurface on Inconel 690TT alloy subjected to fretting wear at elevated temperature.* Materials & Design, 2016. **104**(Supplement C): p. 152-161.
72. Ren, F., P. Bellon, and R.S. Averback, *Nanoscale self-organization reaction in Cu–Ag alloys subjected to dry sliding and its impact on wear resistance.* Tribology International, 2016. **100**: p. 420-429.
73. Zhou, J., R.S. Averback, and P. Bellon, *Stability and amorphization of Cu–Nb interfaces during severe plastic deformation: Molecular dynamics simulations of simple shear.* Acta Materialia, 2014. **73**: p. 116-127.
74. Vo, N.Q., J. Zhou, Y. Ashkenazy, D. Schwen, R.S. Averback, and P. Bellon, *Atomic Mixing in Metals Under Shear Deformation.* JOM, 2013. **65**(3): p. 382-389.

Figure captions

Fig. 1 (A) Cross sectional micrograph of Cu-MoS_2-WC composite and (B) a corresponding EDX map showing S distribution, indicative of MoS_2; (C) and (D) high magnification micrographs of the Cu microstructure, consisting of deformed coarse structure and refined structure that was due to dynamic recrystallization during cold spray.

Fig. 2 (A) A typical sliding loop where the imposed and actual sliding amplitude are indicated; (B) a schematic of theoretical contact, showing wear track length and Hertzian contact and the locations of TEM foils that are marked as small rectangles; (C) the top view of the Hertzian contact and sliding, as well as locations of the TEM foils. The gray circle represents initial Hertzian contact, whose diameter is marked by black double-directional arrow, the dark gray indicates the area that was not directly exposed to air during test, the blue double-directional arrow illustrates extension of the wear track; (D) locations of the three TEM foils marked from the actual SD-ND cross-sectional micrograph.

Fig. 3 (A) a SEM micrograph of the SD-ND cross section of the wear track, where third body layer, subsurface layer and UFG layer are identified; (B) a low magnification TEM image of the subsurface microstructure from TD-ND view. The dark contrast is WC particles; (C) a TEM micrograph (TD-ND cross section) of the UFG structure, showing equiaxed grains with embedded shear bands; (D) EDX line scan across the nanolamellae and UFGs shows Cu and O distributions.

Fig. 4 (A) a bright and (B) a dark field TEM images of the wear-resistant subsurface layer from TD-ND view; (C) a SAED pattern from the nanolamellae, and it is identified as Cu. The intensive diffraction spots are arrowed; (D) distribution of the lamella thickness; (E) a closer view of the nanolamellae, in which the dark contrast (white arrows) indicates dislocations.

Fig. 5 (A) an HRTEM image of two lamellae, referring as I and II. The white arrows mark their interface, whose misorientation was measured using IFFT showed in (B); (C) (D) (E) and (F) exhibit IFFT images of regions C, D, E, and F marked in (A) and were used to measure misorientation inside the lamellae.

Fig. 6 (A) an HRTEM image of a lamella showing defects in the lamella interior; (B) IFFT image of the area marked as B in (A), exhibits SFs; (C) a high magnification of area C in (A), shows presence of a thin twin.

Fig.7 (A) an HRTEM image of the nanolamellae, showing bulging out of the serrated lamella boundary by SFs, whose IFFT and FFT images are shown in (C), as well as a nuclei (marked as red dashed lines) of a recrystallized grain at the triple junction; (B) an HRTEM image of an example in which the serrated lamella was separated from the parent lamella by twinning, whose IFFT and FFT images are in (D), forming a triple junction where a recrystallized grain was nucleated. The white dashed lines indicate lamella boundaries, the black arrows SF boundary, the white arrow twin boundary.

Fig. 8 (A) top view morphology of the indents obtained from Berkovich tip to achieve the hardness value of the nanolamellae; (B) a plot of hardness versus grain size mines square root using our data and previously reported data [33-35]; (C) top view morphology of an indent produced by a cube corner tip to purposely generate pile-ups. The black arrows indicate shear steps.

Fig. 9 (A) a SD-ND cross section of the wear track, showing location of the TEM foil; (B) a SEM micrograph of the third body from TD-ND cross section. Pores are commonly observed inside the third body. (C) an HRTEM image of a third body particle, in which lamella boundary is indicated by black dashed lines, while the grain boundaries in the lamella interior are indicated by white dashed lines. Misorientation of the grain boundaries were measured and marked near them. (D) and (E) are IFFT images of two small areas indicated in (C) and there is a misorientation of ~2° between them. (F) an HRTEM image showing formation of a new grain at a triple junction and it is surrounded by high angle grain boundaries.

Fig. 10 (A) an HRTEM image of the third body from center of the wear track; In (B), the lamella boundary was indicated by black dashed lines, and grain boundaries white dashed lines, the misorientations of the grain boundaries were measured and marked; (C) an HRTEM image showing typical microstructure of a lamella adjacent to pores. The arrows indicate larger elongated grains.

Fig. 11 (A) a low magnification TEM image (TD-ND cross section) of the third body that was exposed to air during test; (B) a closer view of the third body layer and UFG Cu, with a sharp yet cohesive interface between them. The inset is SAED pattern of the third body layer; (C) an HRTEM image of Cu nanograins, exhibiting plane distance of 0.25 nm. The inset is FFT of grains I and II; (D) IFFT of I and II, in which partial dislocations follow a full dislocation, marked as a white arrow and a black “T”; (E) in grain III, SFs emitted from grain boundary and extended

toward grain interior; (F) grains IV and V align along a dashed-line arrow, the white arrows denote Moiré patterns.

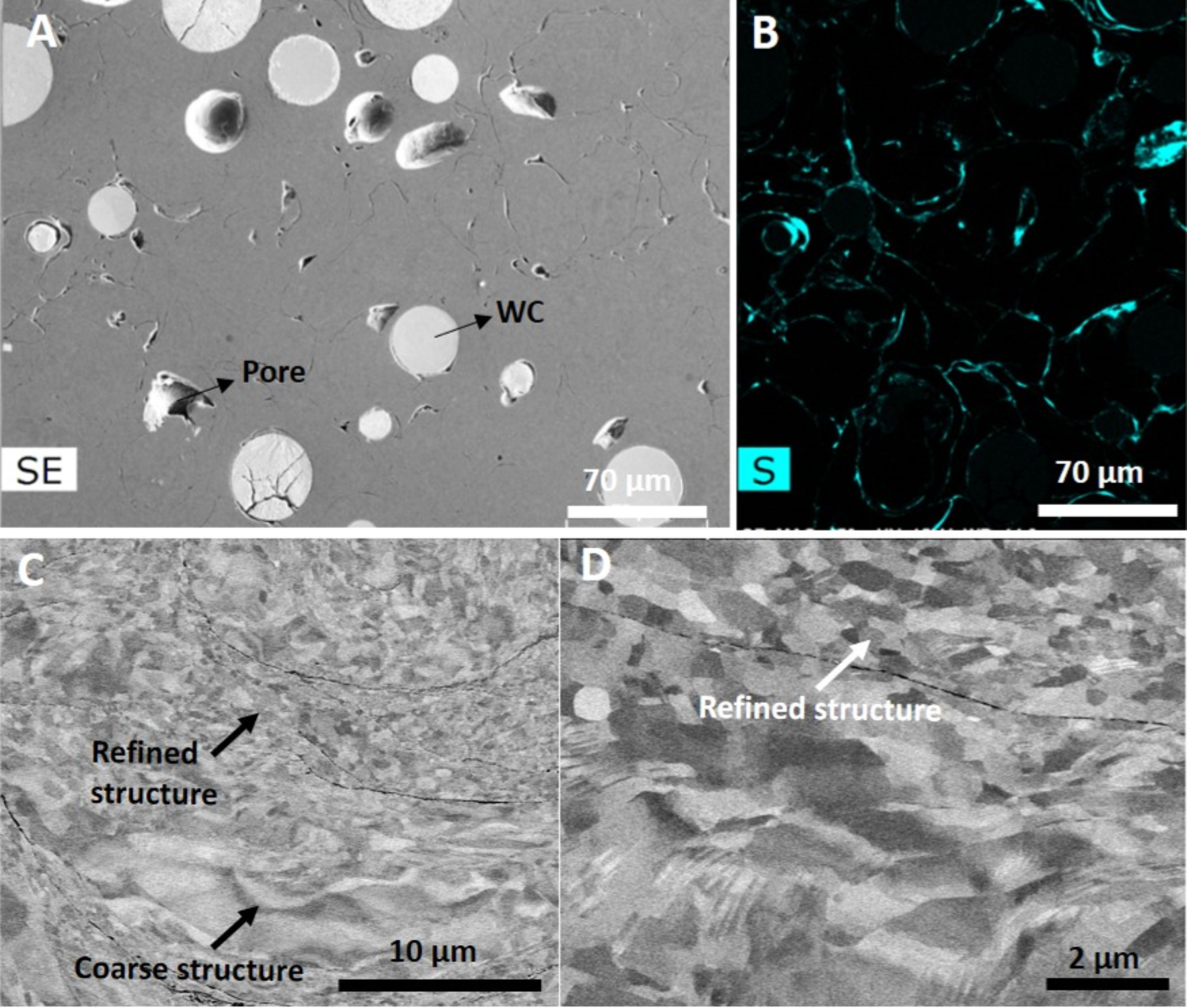
A
WC
Pore
SE
70 µm
B
S
70 µm
C
Refined
structure
Coarse structure
10 µm
D
Refined structure
2 µm

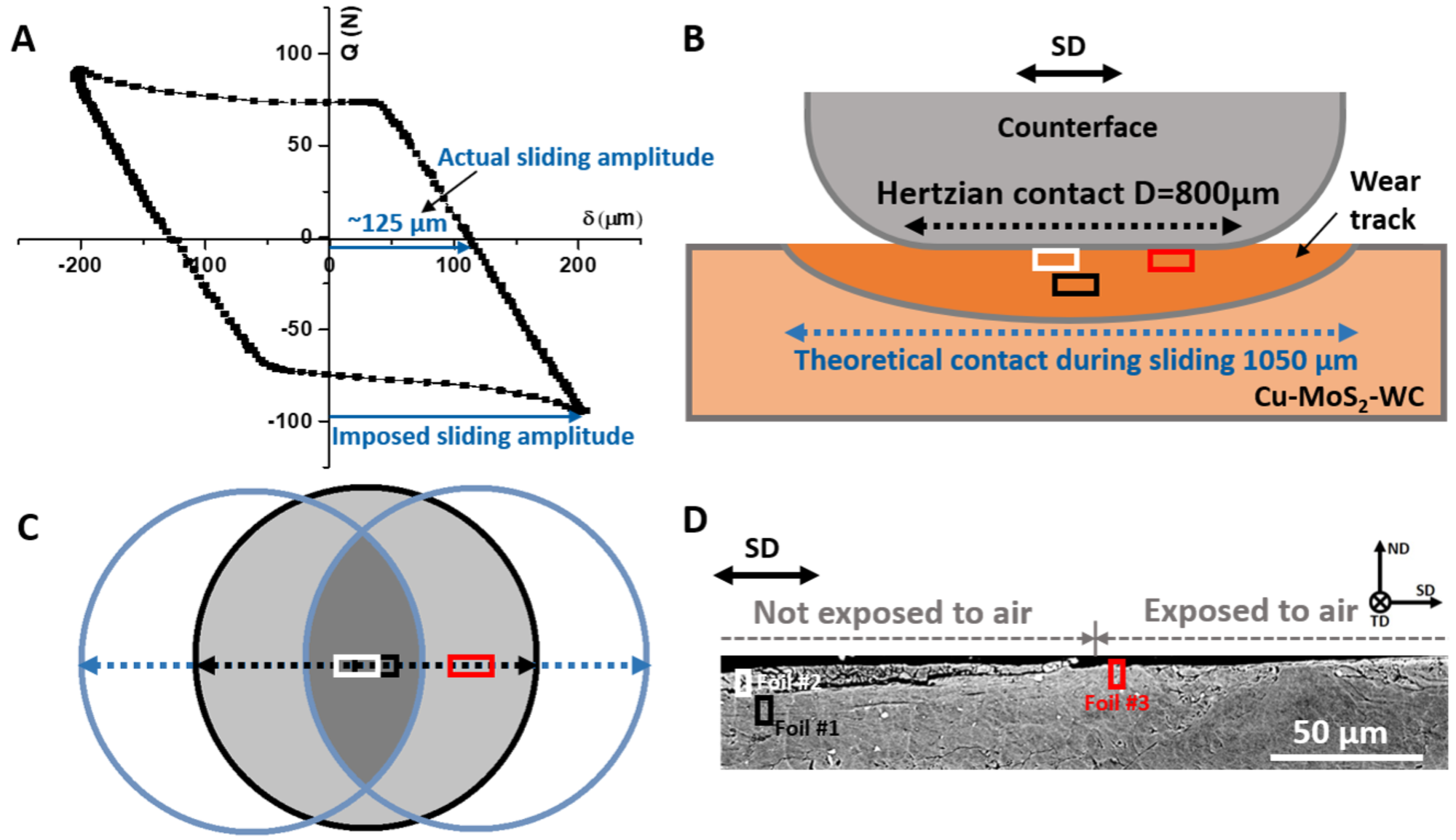
A
Q (N)
100
50
0
-50
-100
-200
-100
0
100
200
δ (µm)
Actual sliding amplitude
~125 µm
Imposed sliding amplitude
B
SD
Counterface
Hertzian contact D=800µm
Wear track
Theoretical contact during sliding 1050 µm
Cu-MoS2-WC
C
D
SD
Not exposed to air
Exposed to air
ND
SD
TD
Foil #2
Foil #1
Foil #3
50 µm

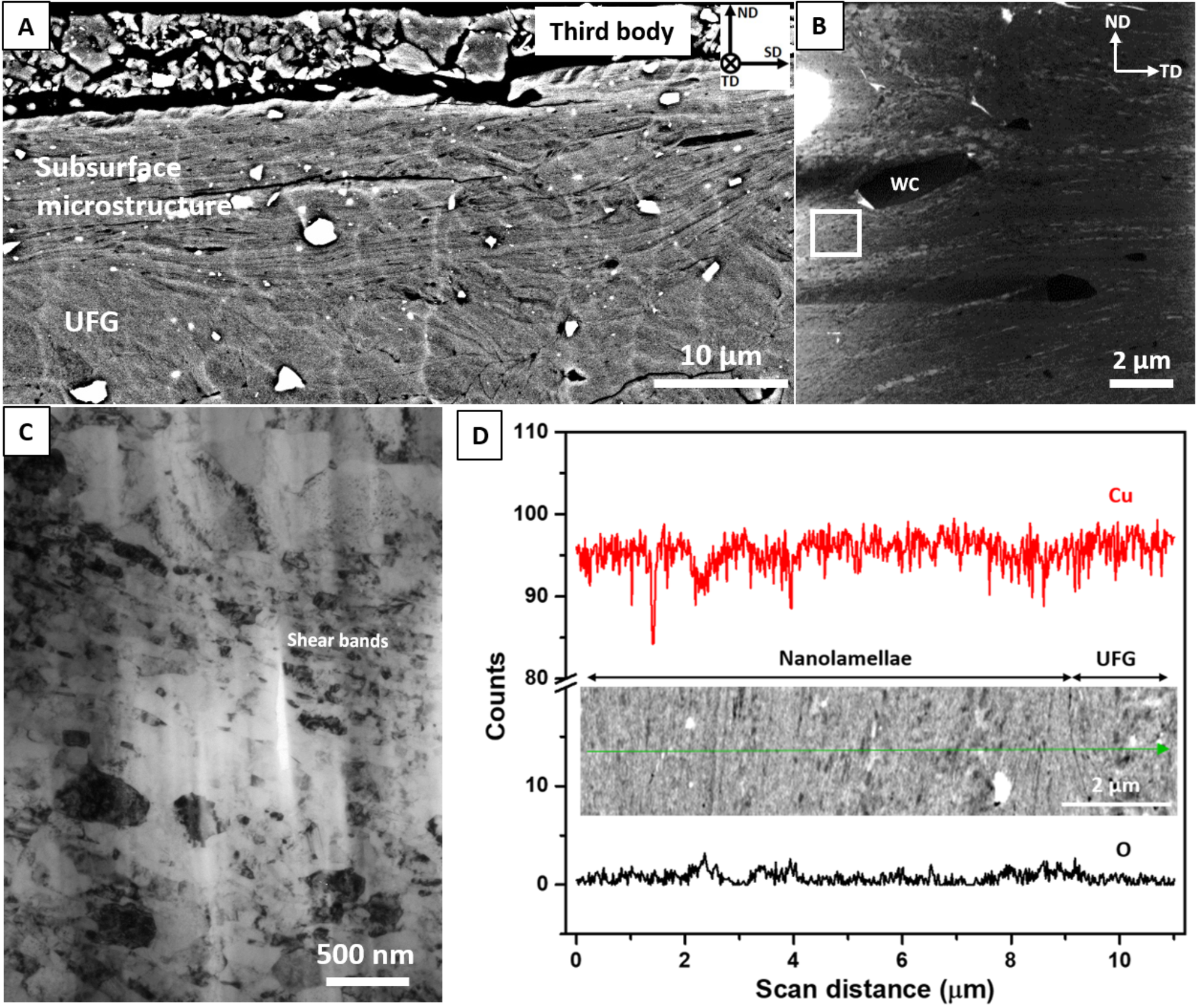
A
Third body
ND
SD
TD
Subsurface
microstructure
UFG
10 µm
B
ND
TD
WC
2 µm
C
Shear bands
500 nm
D
110
100
90
80
10
0
Cu
Nanolamellae
UFG
2 µm
O
Counts
0
2
4
6
8
10
Scan distance (µm)

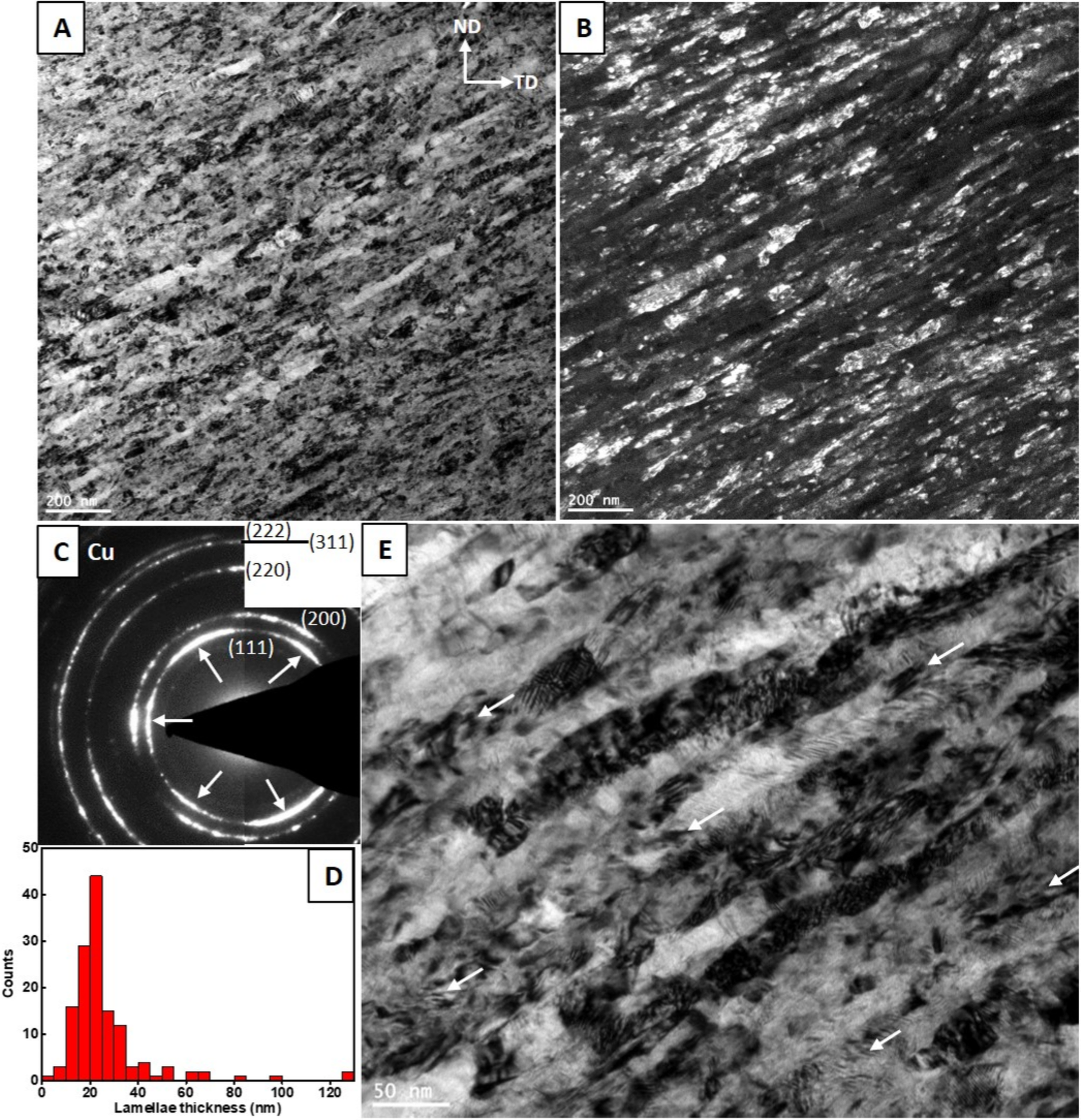
A
ND
TD
200 nm
B
200 nm
C
Cu
(222)
(311)
(220)
(200)
(111)
D
Counts
Lamellae thickness (nm)
0
10
20
30
40
50
0
20
40
60
80
100
120
E
50 nm

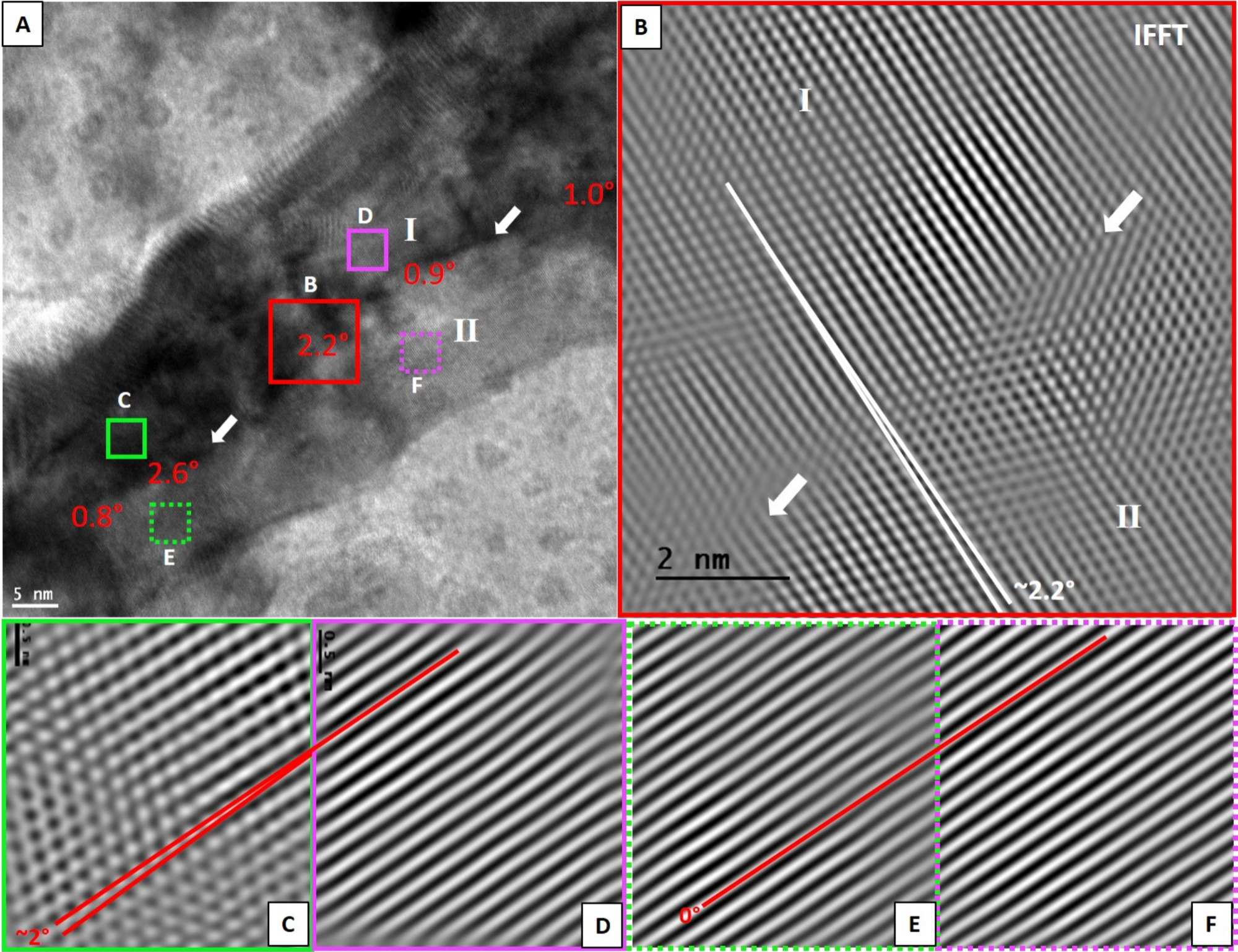
A
1.0°
D
I
0.9°
B
2.2°
II
F
C
2.6°
0.8°
E
5 nm
B
IFFT
I
II
2 nm
~2.2°
C
~2°
D
E
0°
F

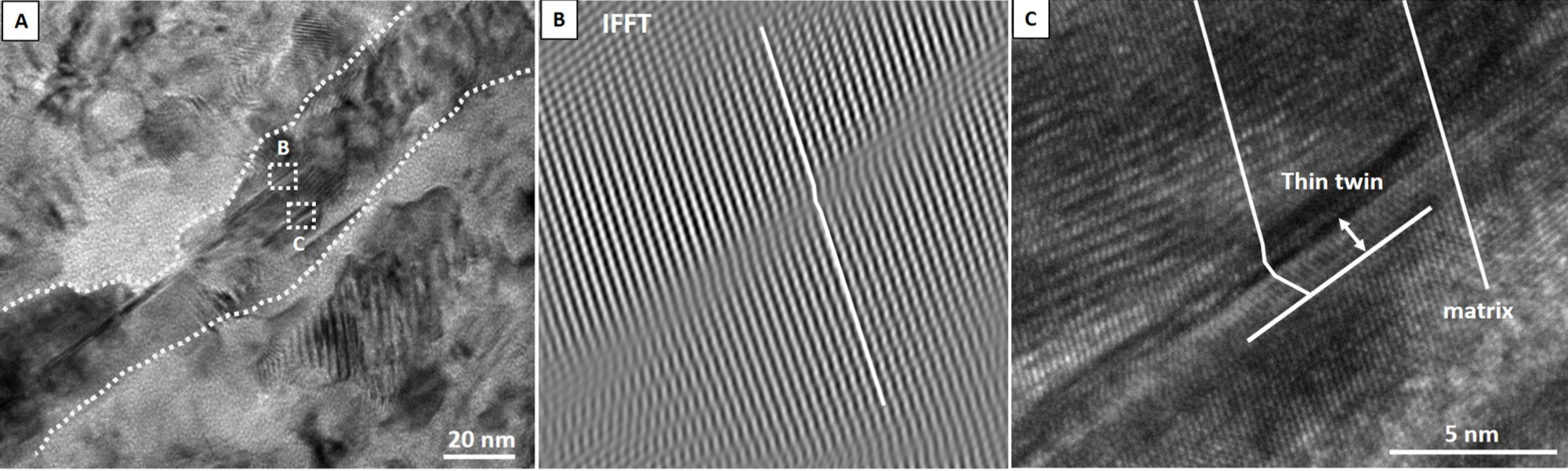
A
B
C
20 nm
B
IFFT
C
Thin twin
matrix
5 nm

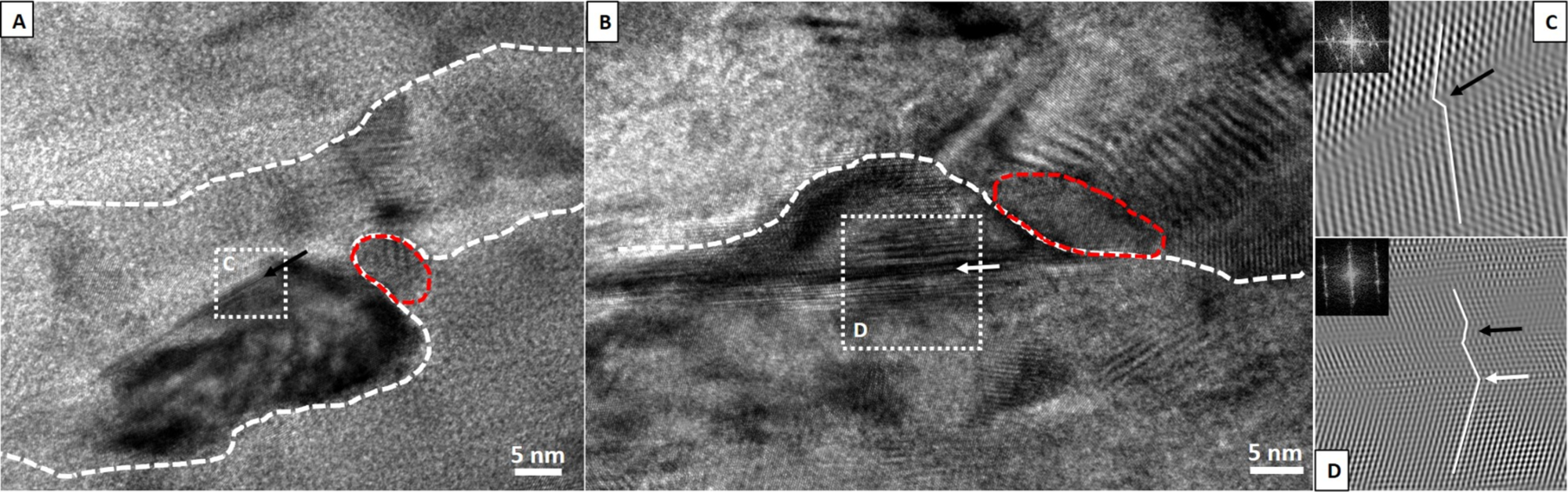
A
C
5 nm
B
D
5 nm
C
D

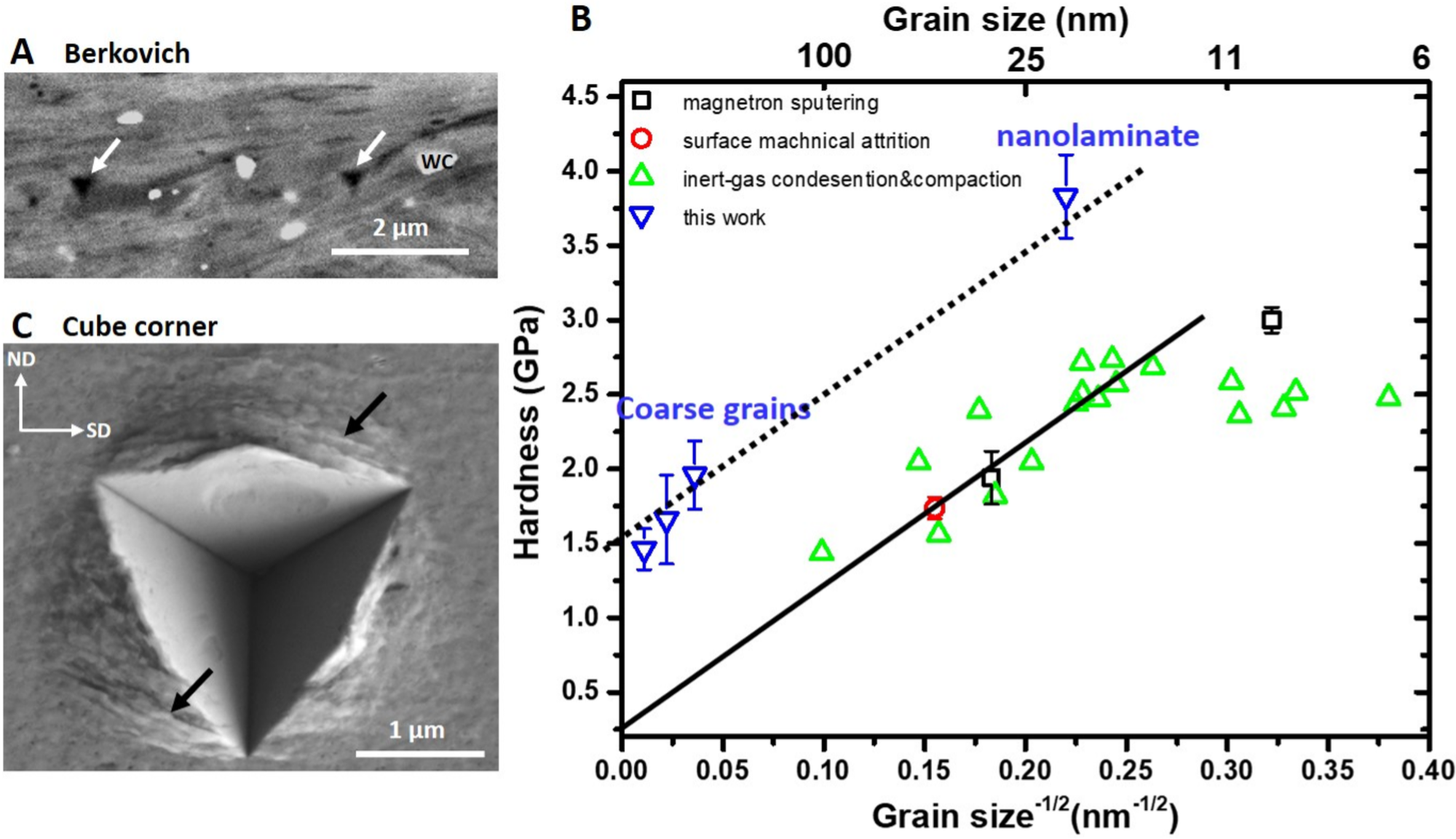
A Berkovich
WC
2 μm
C Cube corner
ND
SD
1 μm
B
Grain size (nm)
100
25
11
6
magnetron sputering
surface machnical attrition
inert-gas condesention&compaction
this work
nanolaminate
Coarse grains
Hardness (GPa)
4.5
4.0
3.5
3.0
2.5
2.0
1.5
1.0
0.5
0.00
0.05
0.10
0.15
0.20
0.25
0.30
0.35
0.40
Grain size$^{-1/2}$(nm$^{-1/2}$)

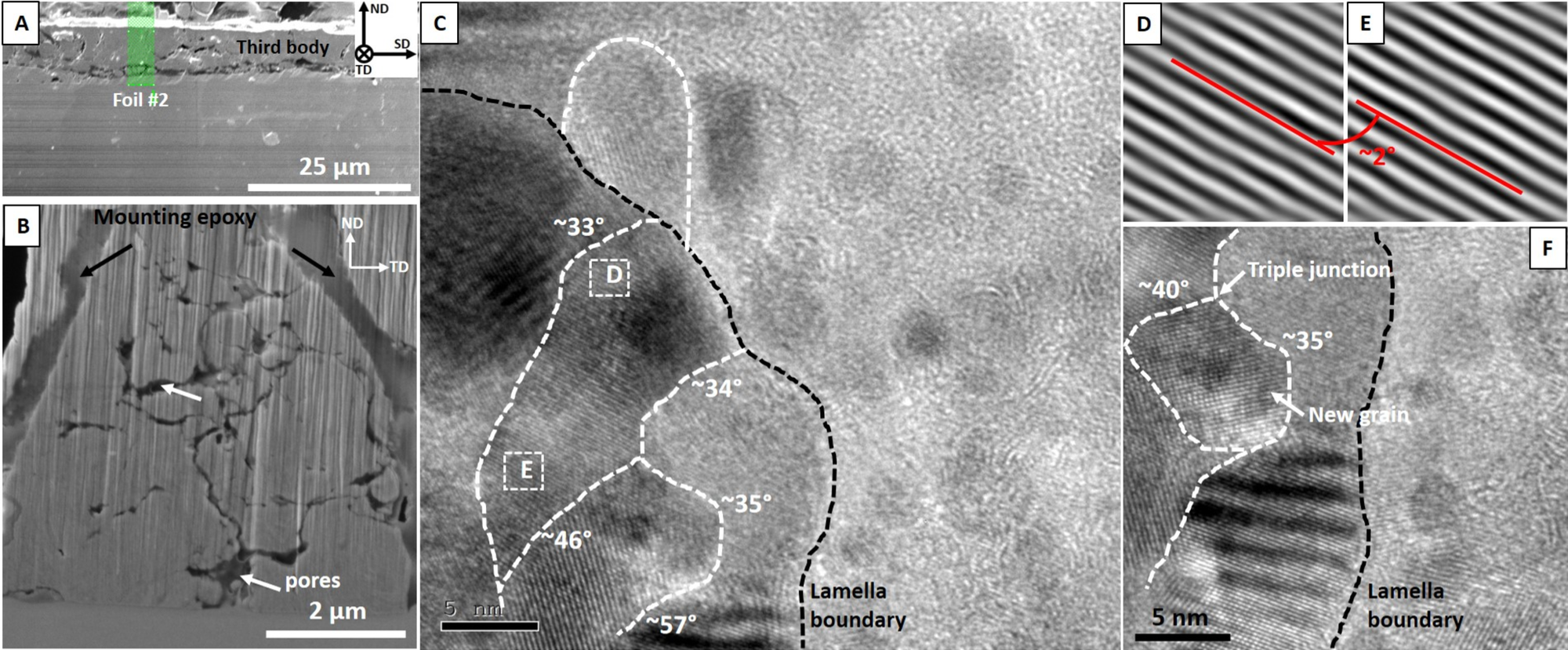
A
Third body
ND
SD
TD
Foil #2
25 µm
B
Mounting epoxy
ND
TD
pores
2 µm
C
~33°
D
~34°
E
~35°
~46°
~57°
5 nm
Lamella boundary
D
E
~2°
F
Triple junction
~40°
~35°
New grain
5 nm
Lamella boundary

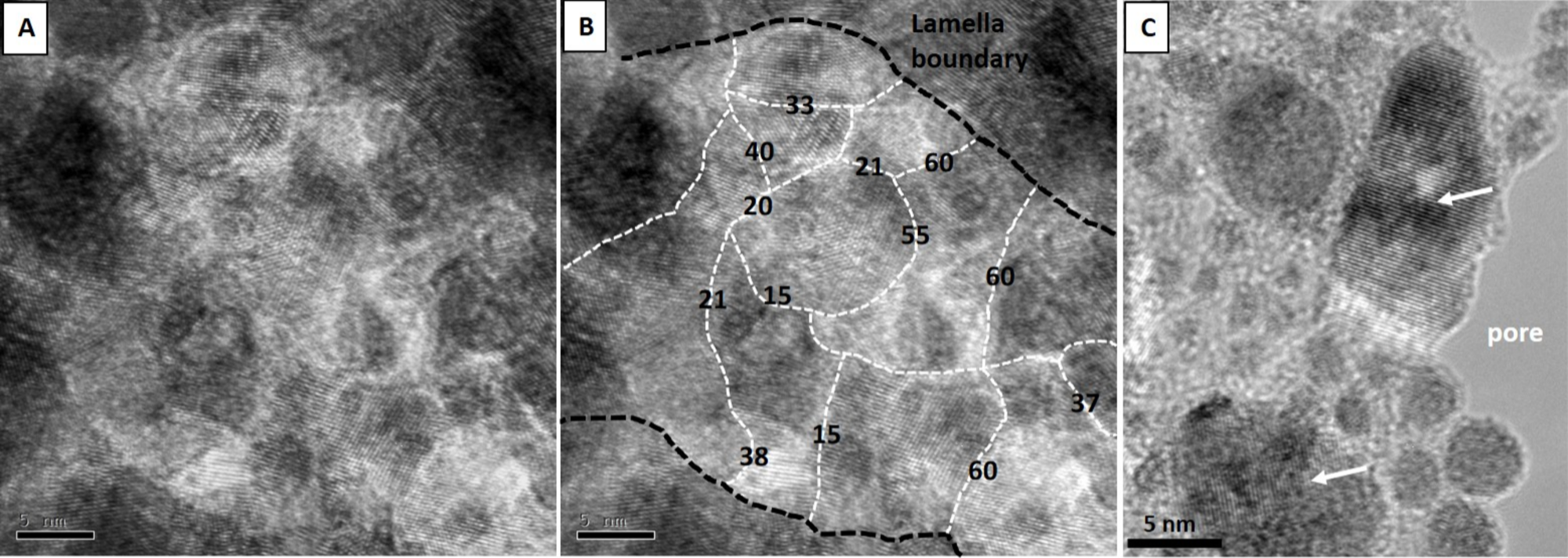
A
5 nm
B
Lamella boundary
33
40
21
60
20
55
60
21
15
37
15
38
60
5 nm
C
pore
5 nm

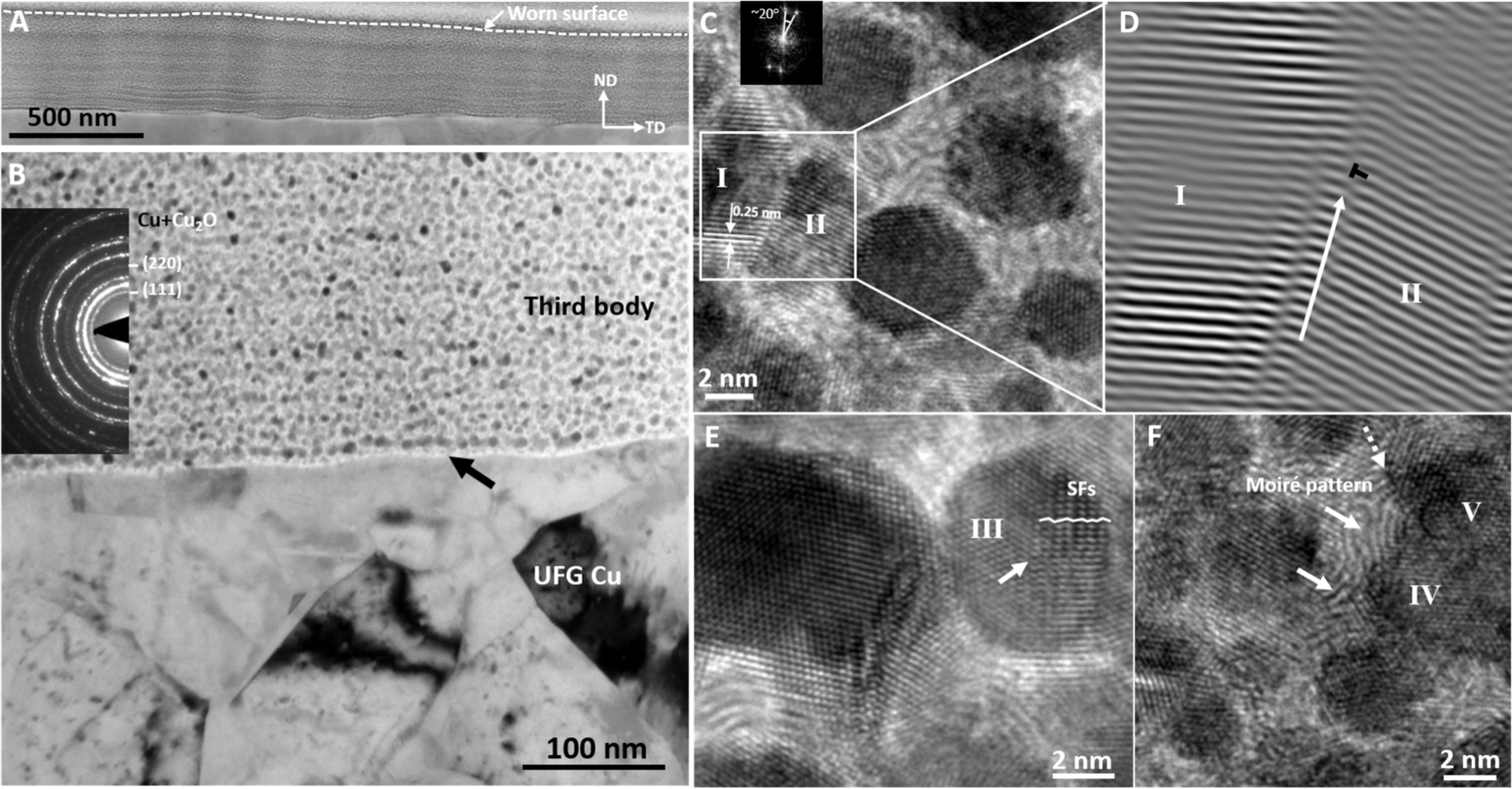
A
Worn surface
ND
TD
500 nm
B
Cu+Cu2O
(220)
(111)
Third body
UFG Cu
100 nm
C
~20°
I
0.25 nm
II
2 nm
D
I
II
E
SFs
III
2 nm
F
Moiré pattern
V
IV
2 nm

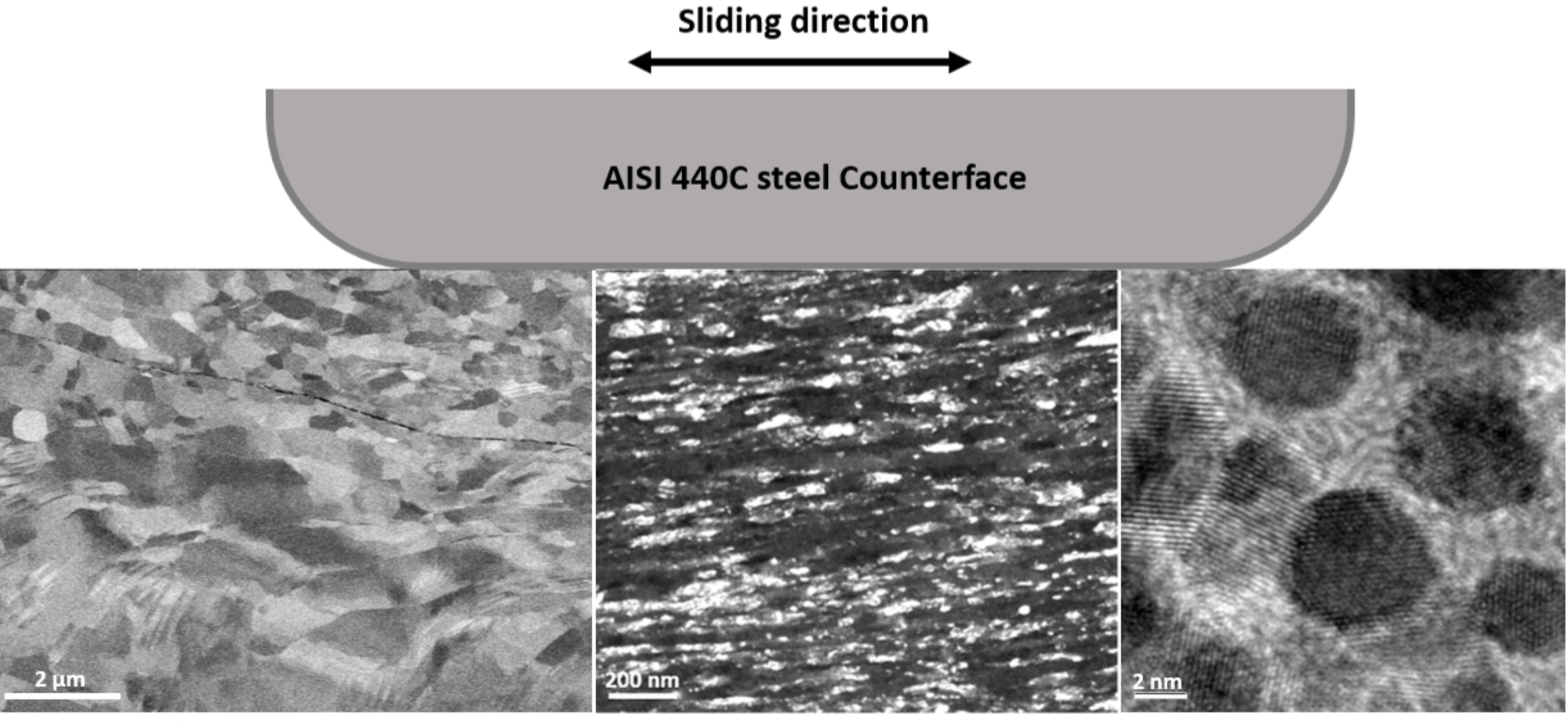
Sliding direction
AISI 440C steel Counterface
2 µm
200 nm
2 nm
Initial microstructure
Subsurface nanolamellae
Top surface nanograins